Monthly Notices
of the
ROYAL ASTRONOMICAL SOCIETY

MNRAS **490,** 4666–4687 (2019)
Advance Access publication 2019 October 12

doi:10.1093/mnras/stz2857

The International Pulsar Timing Array: second data release

B. B. P. Perera,[1,2★] M. E. DeCesar,[3★] P. B. Demorest,[4] M. Kerr,[5] L. Lentati,[6] D. J. Nice,[3] S. Osłowski,[7] S. M. Ransom,[8★] M. J. Keith,[1] Z. Arzoumanian,[9] M. Bailes,[7,10] P. T. Baker,[11,12] C. G. Bassa,[13] N. D. R. Bhat,[14] A. Brazier,[15,16] M. Burgay,[17] S. Burke-Spolaor,[11,12,18] R. N. Caballero,[19] D. J. Champion,[20] S. Chatterjee,[15] S. Chen,[21,22,23,24] I. Cognard,[23,21] J. M. Cordes,[15] K. Crowter,[25] S. Dai,[26] G. Desvignes,[20,27] T. Dolch,[28] R. D. Ferdman,[29] E. C. Ferrara,[30,31] E. Fonseca,[32,33] J. M. Goldstein,[24] E. Graikou,[20] L. Guillemot,[23,21] J. S. Hazboun,[34] G. Hobbs,[26] H. Hu,[20] K. Islo,[35] G. H. Janssen,[13,36] R. Karuppusamy,[20] M. Kramer,[20,1] M. T. Lam,[11,12] K. J. Lee,[37] K. Liu,[20] J. Luo,[38] A. G. Lyne,[1] R. N. Manchester,[39] J. W. McKee,[20,1] M. A. McLaughlin,[11,12] C. M. F. Mingarelli,[40] A. P. Parthasarathy,[7,10] T. T. Pennucci,[41] D. Perrodin,[17] A. Possenti,[17,42] D. J. Reardon,[7,10] C. J. Russell,[43] S. A. Sanidas,[1] A. Sesana,[44] G. Shaifullah,[13] R. M. Shannon,[7,10] X. Siemens,[35,45] J. Simon,[46] R. Spiewak,[7,10] I. H. Stairs,[25] B. W. Stappers,[1] J. K. Swiggum,[35] S. R. Taylor,[47,48] G. Theureau,[23,21,49] C. Tiburzi,[13] M. Vallisneri,[46] A. Vecchio,[24] J. B. Wang,[50] S. B. Zhang,[51,52] L. Zhang,[53,26] W. W. Zhu[54,20] and X. J. Zhu[55]

Affiliations are listed at the end of the paper

Accepted 2019 October 7. Received 2019 September 8; in original form 2019 July 29

ABSTRACT

In this paper, we describe the International Pulsar Timing Array second data release, which includes recent pulsar timing data obtained by three regional consortia: the European Pulsar Timing Array, the North American Nanohertz Observatory for Gravitational Waves, and the Parkes Pulsar Timing Array. We analyse and where possible combine high-precision timing data for 65 millisecond pulsars which are regularly observed by these groups. A basic noise analysis, including the processes which are both correlated and uncorrelated in time, provides noise models and timing ephemerides for the pulsars. We find that the timing precisions of pulsars are generally improved compared to the previous data release, mainly due to the addition of new data in the combination. The main purpose of this work is to create the most up-to-date IPTA data release. These data are publicly available for searches for low-frequency gravitational waves and other pulsar science.

Key words: stars: neutron – pulsars: general – gravitational waves – methods: data analysis.

1 INTRODUCTION

Pulsar timing observations are sensitive to correlated signals at low frequencies, from nHz to μHz, such as those caused by gravitational waves (GWs) produced from inspiraling supermassive black hole binaries (SMBHBs). Millisecond pulsars (MSPs) have been identified as ideal tools for searching for GWs due to their excellent rotational stability (see Detweiler 1979; Hellings & Downs 1983; Jenet et al. 2005). They are old neutron stars that are spun up to spin periods of $\lesssim$20 ms during an accretion phase ('recycling': Alpar et al. 1982; Radhakrishnan & Srinivasan 1982). High-precision timing measurements of many MSPs with sub-microsecond pre-

★ E-mail: bhakthiperera@gmail.com (BBPP); megandecesar@gmail.com (MED); sransom@nrao.edu (SMR)

cision – a Pulsar Timing Array (PTA) – collected over long time spans offer a unique and powerful probe of low-frequency GWs (Arzoumanian et al. 2015b; Desvignes et al. 2016; Reardon et al. 2016). The International Pulsar Timing Array[1] (IPTA) seeks to further improve the sensitivity of PTAs by combining the data from three individual PTAs, namely the European Pulsar Timing Array (EPTA; Desvignes et al. 2016), the North American Nanohertz Observatory for Gravitational Waves (NANOGrav; Arzoumanian et al. 2018a), and the Parkes Pulsar Timing Array (PPTA; Reardon et al. 2016). The combination of all the data from the individual PTAs under the auspices of the IPTA should reduce the time to the detection of GWs: the GWs from the cosmic merger history of SMBHBs should create a GW background which may be detectable in the next 5 yr (Siemens et al. 2013; Rosado, Sesana & Gair 2015; Taylor et al. 2016; Kelley et al. 2017), and GWs from individual SMBHBs in the next 10 yr (Rosado et al. 2015; Mingarelli et al. 2017; Kelley et al. 2018).

The first IPTA data release (IPTA dr1 – Verbiest et al. 2016) reported a combination of timing data of 49 MSPs observed by individual PTAs. The data lengths of these pulsars ranged between 4.5 and 27 yr, depending on when the source was included in the timing campaign. The data release included the timing data from the EPTA until 2013 February, NANOGrav until 2009 October, and the PPTA until 2013 October. Recently, the EPTA (Desvignes et al. 2016), NANOGrav (Arzoumanian et al. 2015b), and the PPTA (Reardon et al. 2016) reported new data releases. Here we report the creation of the IPTA second data release (IPTA dr2) and make it available for GW search experiments and other related science. We note that the recently released NANOGrav 11 yr data set (Arzoumanian et al. 2018a) and the new PPTA dr2 (Kerr et al., in preparation) will be included in future IPTA data releases.

The timing data released by individual PTAs have been used to search for GWs and place upper limits on their strain amplitudes (see Yardley et al. 2010; Arzoumanian et al. 2014; Zhu et al. 2014; Lentati et al. 2015; Shannon et al. 2015; Arzoumanian et al. 2016, 2018a; Babak et al. 2016; Aggarwal et al. 2018; Perera et al. 2018). The IPTA dr1 has also been used in GW search experiments and has placed limits on the stochastic GW background (Verbiest et al. 2016). Furthermore, with a better sky-coverage, Goldstein et al. (2018) addressed the importance of the IPTA data set in localizing resolvable GW sources and reported that the results are superior to what is achieved by individual PTAs. Mingarelli et al. (2018) showed how one can combine IPTA dr1 with Gaia Collaboration (2018) data to improve binary pulsar distance estimates, which can in turn be used to improve PTA sensitivity to individual SMBHB systems (Corbin & Cornish 2010; Lee et al. 2011; Ellis 2013; Taylor, Ellis & Gair 2014; Zhu et al. 2016) and eventually measure their spin (Sesana & Vecchio 2010; Mingarelli et al. 2012). Lentati et al. (2016) showed the importance of the IPTA dr1 by studying the noise processes of pulsars to improve their timing stabilities. Therefore, a more up-to-date IPTA data combination is crucial to improve the timing precision and thus, the sensitivity of pulsars to GWs, leading towards a detection in the near future. In addition to the search for GWs, the IPTA data set has been used in other areas of astrophysics. For example, Caballero et al. (2018) utilized the IPTA dr1 to study the Solar system and provided improved PTA mass estimates for planetary systems, the first PTA-based estimates of asteroid-belt object masses, such as the dwarf planet Ceres, and provided generic mass limits for unknown objects in orbits in the Solar system, including theoretical objects such as dark matter clumps.

Verbiest et al. (2016) described the pulsar timing, procedure for creating and combining IPTA data sets, and the usage of the IPTA data comprehensively. The process of the new data combination here in IPTA dr2 is broadly similar to that of the IPTA dr1 and thus we only briefly overview the combination procedure in this paper, and refer the reader to Verbiest et al. (2016) for additional details. The paper is organized as follows: we first describe the constituent PTA data sets used in this combination in Section 2. The data combination procedure is briefly described in Section 3 and the final data products are presented in Section 4. We discuss our results and compare with the results of IPTA dr1 in Section 5. Finally in Section 6, we discuss the future projects that will be carried out using this new IPTA data release.

2 DATA SETS

To produce the IPTA dr2, we combined published data from recent individual PTA data releases, along with a selection of additional data sets that were either used in the IPTA dr1 or published in other studies. Detailed descriptions of each of these data sets are given below.

EPTA data set: We include the most recent EPTA data release 1.0 (Desvignes et al. 2016) in the IPTA dr2. This data set includes high-precision timing observations from 42 MSPs obtained with the Effelsberg Radio Telescope (EFF) in Germany, the Lovell Radio Telescope at the Jodrell Bank Observatory (JBO) in the UK, the Nançay Radio Telescope (NRT) in France, and the Westerbork Synthesis Radio Telescope (WSRT) in the Netherlands. The data set spans timing baselines of 7–18 yr, covering from 1996 October to 2015 January. In addition, we note that the data set of PSR J1939+2134 includes very early NRT observations that started in 1990 March. Each observation is averaged both in time and frequency, across the bandwidth, and provides a single time-of-arrival (ToA). Observation information is given in Table 1 and additional details can be found in Desvignes et al. (2016).

NANOGrav data set: We include the NANOGrav 9 yr data set (Arzoumanian et al. 2015b) in this data combination. This includes high-precision timing observations obtained from 37 MSPs, with timing baselines between 0.6 and 9.2 yr from 2004 July to 2013 March. We also include the long-term NANOGrav timing data of PSR J1713+0747 reported in Zhu et al. (2015), and the data of PSRs J1857+0943 and J1939+2134 from 1984 November through 1992 December reported in Kaspi, Taylor & Ryba (1994). All of these observations were obtained using the Robert C. Byrd Green Bank Telescope (GBT) and the Arecibo Observatory (AO) in the USA. We note that the ToAs in the NANOGrav 9 yr data set are obtained by first averaging the observations in time as given in Arzoumanian et al. (2015b), and in frequency such that the data maintain a frequency resolution (i.e. sub-band information) ranging from 1.5 to 12.5 MHz depending on the combination of receiver and backend.[2] Each frequency channel yields a single ToA. The observations in Zhu et al. (2015) are partially averaged in time and frequency, resulting in multiple ToAs for a given observation epoch. The observations in Kaspi et al. (1994) are fully averaged in

[1] http://ipta4gw.org

[2] The frequency channel bandwidths in the NANOGrav 9-yr data set are: ASP/GASP: 4 MHz at all frequencies; PUPPI/GUPPI: 1.6 MHz at below 500 MHz; 3.1 MHz between 500 and 1000 MHz; and 12.5 MHz above 1000 MHz.

Table 1. The observation information in PTA data releases. Note that, as in IPTA dr1, the GBT and AO observations of PSR J1713+0747 reported in Zhu et al. (2015) and early AO observations of PSRs J1857+0943 and J1939+2134 reported in Kaspi et al. (1994) are included in the data combination.

PTA	Telescope	Typical cadence (weeks)	No. of pulsars	Observing frequencies (GHz)	Data span (MJD/Gregorian) Earliest−latest
EPTA	EFF	4	18	1.4, 2.6	50360 (1996 Oct 4)–56797 (2014 May 20)
	JBO	3	35	1.4	54844 (2009 Jan 13)−57028 (2015 Jan 6)
	NRT	2	42	1.4, 2.1	47958 (1990 Mar 8)−56810 (2014 Jun 2)
	WSRT	4	19	0.3, 1.4, 2.2	51386 (1999 Jul 27)−55375 (2010 Jun 28)
NANOGrav	GBT	4	20	0.8, 1.4	53216 (2004 Jul 30)−56598 (2013 Nov 2)
	AO	4	19	0.3, 0.4, 1.4, 2.3	53343 (2004 Dec 4)−56599 (2013 Nov 3)
Zhu et al. (2015)	GBT and AO	2	1	0.8, 1.4, 2.3	48850 (1992 Aug 16)−56598 (2013 Nov 2)
Kaspi et al. (1994)	AO	2	2	1.4, 2.3	46436 (1986 Jan 6)−48973 (1992 Dec 17)
PPTA	PKS	2	20	0.6, 1.4, 3.1	49373 (1994 Jan 21)−57051 (2015 Jan 29)

time and frequency, leading to one ToA for each receiver and data acquisition system at each epoch.

PPTA data set: We include the PPTA first data release (Manchester et al. 2013) and its extended version (Reardon et al. 2016) in this IPTA data combination. This PPTA data set includes high-precision timing observations obtained from 20 MSPs with an observation time baseline of approximately 6 yr. Additional 'legacy' *L*-band (i.e. 1400 MHz) observations acquired between 1994 and 2005, for which the raw data are no longer available, are also included in the combination. Finally, we include more recent PPTA observations reported in Shannon et al. (2015) for the high-precision PSRs J0437−4715, J1744−1134, J1713+0747, and J1909−3744. All the PPTA observations are obtained using the Parkes Radio Telescope in Australia and a range of receivers and pulsar timing backends. Although the ToA coverage is nearly identical to the data sets indicated above, the raw data from 2005 onwards have been reprocessed using a pipeline developed for new PPTA data releases (Kerr et al. in preparation). In general, PPTA data are divided into four bands with wavelengths of roughly 10, 20, 40, and 50 cm. An analytic template for the pulse profile for each instrument and band is produced, and the unknown phase offset between these templates is measured from the data as a free parameter in the timing model. Instrumental offsets ('JUMPs') were obtained using a modulated PIN diode as described in Manchester et al. (2013). Similar to the EPTA data set, each observation of the PPTA data set is averaged in time and frequency, resulting in a single ToA for each radio receiver at each epoch.

Combining all the above mentioned data sets, the new IPTA data release comprises 65 pulsars in total, adding 16 new pulsars compared to IPTA dr1. All of these new pulsars are observed and included by the NANOGrav timing campaign. By comparing positions, it is evident that these new pulsars improved the IPTA pulsar distribution in the Galaxy, providing a better sky coverage compared to the previous data release (see Fig. 1). A summary of the data sets used in this data release is given in Table 1 and the basic parameters of these MSPs are given in Table 2. Fig. 2 shows the frequency coverages and the time baselines of these data sets in the data combination.

3 CREATING THE IPTA DR2 DATA SET

We combine ToA measurements from individual PTA data releases into a single data set, and then perform the timing analysis for each pulsar in that data set. In this work, we always use ToAs as reported

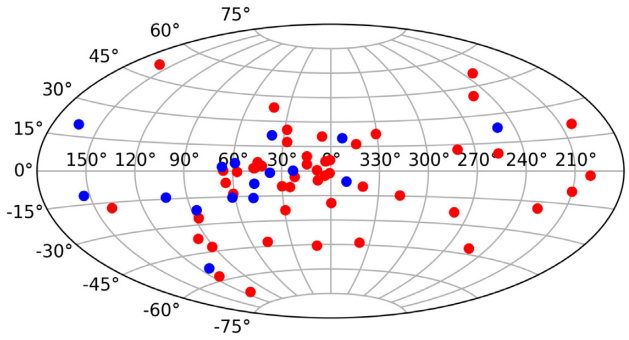

Figure 1. The Galactic distribution of 65 pulsars in the data release, including 49 pulsars from the IPTA dr1 (*red* dots) and 16 new pulsars (*blue* dots) that were not presented in the IPTA dr1. Galactic latitude is on the vertical axis in degrees, and Galactic longitude is on the horizontal axis in degrees, increasing leftward with the Galactic Centre at the origin. Note that many new pulsars included in this data release fill some gaps in the IPTA dr1 pulsar distribution.

in the individual PTA data sets, i.e. we have not re-processed raw observational data. When possible, we include metadata (such as observation time and bandwidth) either as reported in the individual PTA data set or extracted from the original raw data files. In some cases (e.g. early WSRT observations and the data reported in Kaspi et al. 1994), it was not possible to recover a full set of metadata.

The data combination procedure is detailed in Verbiest et al. (2016), and we summarize it here. We use the pulsar timing software package TEMPO2[3] (Edwards, Hobbs & Manchester 2006; Hobbs, Edwards & Manchester 2006) to fit the timing model to the observed ToAs and obtain timing residuals (i.e. the difference between the observed and predicted ToAs) of the pulsar. We combine the different data sets of a given pulsar by fitting for time offsets (or 'JUMPs') in the timing model to account for any systematic delays between them (see Verbiest et al. 2016). We define the highest weighted data set (i.e. the sum of $1/\sigma^2$, where σ is the ToA uncertainty) as the reference data set (i.e. JUMP is equal to zero) in the timing model of the pulsar and then include separate JUMPs for each of other data sets to constrain their time offsets with respect to the reference. We note that, as mentioned in Section 2,

[3] https://bitbucket.org/psrsoft/tempo2

Table 2. The basic properties of the pulsars in the IPTA second data release. The sources in this new data release that were not in IPTA dr1 are marked with '*'. The flux density of the pulsar at 1.4 GHz is quoted in the fourth column. The distance to the pulsar is given in fifth column, using the electron density model YMW16 (Yao, Manchester & Wang 2017) based on the timing measured DM value, or compiled by the model given in Verbiest et al. (2012), either using the updated parallax measurement from this paper (denoted by † – see Appendix A) or from previously published parallax measurements[a] (denoted by ‡). The uncertainty of the DM-derived distance is estimated considering a typical 20 per cent error of the electron density model. The next columns indicate with an 'X' whether the pulsar is observed by that particular PTA. The ninth column presents if the DM model given in Keith et al. (2013) is included (Y) or excluded (N) in the timing solution of the pulsar according to VersionA (see Section 4.1). In the tenth column, we quote the weighted root mean square of the timing residuals σ_w, after subtracting out the timing model and the maximum likelihood time-correlated signals reported in VersionB (see Section 4.2). The eleventh column gives the time span of the data set.

PSR	Pulse period (ms)	DM (cm^{-3} pc)	$S_{1.4}$ (mJy)	Distance (kpc)	EPTA	NANOGrav	PPTA	DM_k	σ_w (μs)	Span (year)	References
J0023+0923*	3.050	14.33	0.5	1.2 ± 0.2		X		Y	1.34	2.3	1, 2, 3
J0030+0451	4.865	4.33	0.6	0.34 ± 0.01†	X	X		Y	1.48	15.1	4, 2, 3
J0034−0534	1.877	13.77	0.6	1.03 ± 0.3	X			N	4.19	13.5	5, 6, 7
J0218+4232	2.323	61.25	0.9	$3.7^{+1.1}_{-0.8}$‡	X			Y	7.01	17.6	8, 9, 10, 11, 12
J0340+4130*	3.299	49.58	0.3	1.6 ± 0.3		X		Y	5.16	1.7	1, 2, 3
J0437−4715	5.757	2.64	149.0	0.156 ± 0.001‡			X	Y	0.11	18.6	13, 14, 15, 16, 17
J0610−2100	3.861	60.67	0.4	3.3 ± 0.7	X			N	4.88	6.9	18
J0613−0200	3.062	38.78	2.3	1.11 ± 0.05†	X	X	X	Y	1.14	16.0	19, 2, 20, 21
J0621+1002	28.854	36.47	1.9	0.4 ± 0.1	X			Y	6.57	11.8	22, 9, 11
J0645+5158*	8.853	18.25	0.3	0.7 ± 0.1		X		Y	0.57	2.4	23, 2, 3
J0711−6830	5.491	18.41	3.2	0.11 ± 0.02			X	Y	1.44	17.1	24, 14, 20, 16
J0751+1807	3.479	30.25	3.2	$1.4^{+0.4}_{-0.3}$‡	X			N	3.00	17.6	25, 9, 11, 26
J0900−3144	11.110	75.71	3.8	0.4 ± 0.1	X			N	3.21	6.9	18, 9, 16
J0931−1902*	4.638	41.49	0.4	3.7 ± 0.7		X		N	3.69	0.6	27, 2, 3
J1012+5307	5.256	9.02	3.2	$0.8^{+0.2}_{-0.1}$‡	X	X		Y	1.91	16.8	28, 29, 3
J1022+1001	16.453	10.25	6.1	0.72 ± 0.02‡	X		X	Y	1.97	17.5	22, 14, 20, 21, 30
J1024−0719	5.162	6.49	1.5	$1.2^{+0.2}_{-0.1}$†	X	X	X	Y	1.71	18.2	24, 2, 16
J1045−4509	7.474	58.14	2.7	$0.5^{+1.3}_{-0.3}$‡			X	Y	3.19	17.0	5, 14, 16, 31
J1455−3330	7.987	13.57	1.2	$1.0^{+0.3}_{-0.2}$‡	X	X		Y	4.12	9.7	19, 2, 7, 26
J1600−3053	3.598	52.32	2.5	$2.0^{+0.3}_{-0.2}$†	X	X	X	Y	0.92	12.3	32, 2, 21
J1603−7202	14.842	38.05	3.1	1.1 ± 0.2			X	Y	1.58	15.3	33, 14, 20, 21
J1614−2230*	3.151	34.49	0.7	$0.69^{+0.05}_{-0.04}$†		X		Y	1.38	5.1	34, 2, 3
J1640+2224	3.163	18.42	2.0	1.5 ± 0.3	X	X		Y	0.77	17.2	2, 11
J1643−1224	4.622	62.41	4.8	$1.1^{+0.6}_{-0.3}$†	X	X	X	Y	2.55	20.1	19, 14, 21
J1713+0747	4.570	15.97	10.2	1.20 ± 0.03†	X	X	X	Y	0.21	22.5	35, 2, 21
J1721−2457	3.497	47.76	0.6	1.4 ± 0.3	X			N	12.21	12.8	36, 37
J1730−2304	8.123	9.62	3.9	$0.60^{+0.09}_{-0.07}$†	X		X	Y	1.57	20.3	19, 14, 16
J1732−5049	5.313	56.82	1.3	1.87 ± 0.4			X	Y	2.72	8.0	36, 14, 21
J1738+0333	5.850	33.77	0.7	1.5 ± 0.1‡	X	X		Y	1.38	7.3	38, 39, 3
J1741+1351*	3.747	24.20	0.9	1.4 ± 0.3		X		Y	0.46	4.2	32, 2
J1744−1134	4.075	3.137	3.1	0.410 ± 0.008†	X	X	X	Y	0.73	19.9	24, 14, 16
J1747−4036*	1.646	152.98	0.9	7.1 ± 1.4		X		Y	4.79	1.7	40, 2, 41
J1751−2857	3.915	42.84	0.1	1.1 ± 0.2	X			N	2.85	8.3	42, 9
J1801−1417	3.625	57.26	0.2	1.1 ± 0.2	X			N	2.76	7.0	43, 9, 44
J1802−2124	12.648	149.63	0.8	3.0 ± 0.6	X			N	2.76	7.2	43, 45
J1804−2717	9.343	24.67	0.4	0.8 ± 0.2	X			N	3.72	8.4	33, 9, 10, 11
J1824−2452A	3.054	119.89	2.0	3.7 ± 0.7			X	Y	0.57	5.6	46, 14, 21
J1832−0836*	2.719	28.18	1.1	0.8 ± 0.2		X		Y	1.86	0.6	47, 2
J1843−1113	1.846	59.96	0.1	1.7 ± 0.3	X			N	0.71	10.0	48, 9
J1853+1303	4.092	30.57	0.4	1.3 ± 0.3	X	X		Y	1.31	8.4	43, 2, 42
J1857+0943	5.362	13.30	5.0	1.1 ± 0.1†	X	X	X	Y	1.16	28.4	49, 2, 21
J1903+0327*	2.150	297.52	1.3	6.1 ± 1.2		X		Y	2.11	4.0	50, 51
J1909−3744	2.947	10.39	2.1	1.14 ± 0.01†	X	X	X	Y	0.19	10.8	52, 14, 16
J1910+1256	4.984	38.07	0.5	1.5 ± 0.3	X	X		Y	1.42	9.5	43, 2, 42
J1911−1114	3.626	31.02	0.5	1.1 ± 0.2	X			N	4.30	7.5	33, 9, 11
J1911+1347	4.626	30.99	0.1	1.4 ± 0.3	X			N	1.09	8.8	43, 2, 44
J1918−0642	7.646	26.55	0.6	$1.3^{+0.2}_{-0.1}$†	X	X		Y	1.80	12.8	36, 2, 37
J1923+2515*	3.788	18.86	0.2	1.2 ± 0.2		X		Y	2.25	2.2	53, 2, 3
J1939+2134	1.558	71.02	13.2	$4.7^{+1.4}_{-0.9}$†	X	X	X	Y	0.24	29.4	54, 9, 21
J1944+0907*	5.185	24.34	2.6	1.2 ± 0.2		X		Y	2.22	5.7	55, 2, 3
J1949+3106*	13.138	164.13	0.2	7.5 ± 1.5		X		Y	4.61	1.2	56

Table 2 – *continued*

PSR	Pulse period (ms)	DM (cm^{-3} pc)	$S_{1.4}$ (mJy)	Distance (kpc)	EPTA	NANOGrav	PPTA	DM_k	σ_w (μs)	Span (year)	References
J1955+2908	6.133	104.50	1.1	6.3 ± 1.3	X	X		Y	3.20	8.1	57, 2, 11
J2010−1323	5.223	22.16	1.6	$1.9^{+0.8}_{-0.5}$‡	X	X		Y	2.53	7.4	32, 2, 30
J2017+0603*	2.896	23.92	0.5	1.4 ± 0.3		X		Y	0.72	1.7	58, 2
J2019+2425	3.934	17.20	–	1.2 ± 0.2	X			N	9.64	9.1	59, 60
J2033+1734	5.949	25.08	–	1.7 ± 0.3	X			N	13.65	7.9	61, 2
J2043+1711*	2.380	20.71	–	1.1 ± 0.1†		X		Y	0.63	2.3	1, 2
J2124−3358	4.931	4.60	3.6	$0.39^{+0.05}_{-0.04}$†	X		X	Y	2.89	20.0	24, 14, 21
J2129−5721	3.726	31.85	1.1	$0.6^{+0.6}_{-0.2}$‡			X	Y	0.98	15.4	33, 14, 21, 31
J2145−0750	16.052	9.00	8.9	0.62 ± 0.02‡	X	X	X	Y	1.73	21.2	5, 9, 14, 16, 30
J2214+3000*	3.119	22.55	0.5	0.9 ± 0.2†		X		Y	1.67	2.1	62, 2, 3
J2229+2643	2.978	22.72	0.9	1.8 ± 0.4	X			N	4.28	8.2	63, 2, 11
J2302+4442*	5.192	13.73	1.2	0.9 ± 0.2		X		Y	5.82	1.7	58, 27
J2317+1439	3.445	21.90	4	$0.7^{+0.7}_{-0.3}$‡	X	X		Y	0.87	17.3	64, 2, 11, 30
J2322+2057	4.808	13.36	–	1.0 ± 0.2	X			N	6.74	7.9	59, 9

Notes. [a]http://hosting.astro.cornell.edu/research/parallax/.

References: (1) Hessels et al. (2011), (2) Arzoumanian et al. (2018a), (3) Levin et al. (2016), (4) Lommen et al. (2000), (5) Bailes et al. (1994), (6) Abdo et al. (2010), (7) Toscano et al. (1998), (8) Navarro et al. (1995), (9) Desvignes et al. (2016), (10) Hobbs et al. (2004b), (11) Kramer et al. (1998), (12) Du et al. (2014), (13) Johnston et al. (1993), (14) Reardon et al. (2016), (15) Verbiest et al. (2008), (16) Jankowski et al. (2018), (17) Deller et al. (2008),d (18) Burgay et al. (2006), (19) Lorimer et al. (1995), (20) Hotan, Bailes & Ord (2006), (21) Manchester et al. (2013), (22) Camilo et al. (1996), (23) Stovall et al. (2014), (24) Bailes et al. (1997), (25) Lundgren, Zepka & Cordes (1995), (26) Guillemot et al. (2016), (27) Arzoumanian et al. (2015b), (28) Nicastro et al. (1995), (29) Lazaridis et al. (2009), (30) Deller et al. (2019), (31) Verbiest et al. (2009), (32) Jacoby et al. (2007), (33) Lorimer et al. (1996), (34) Crawford et al. (2006) (35) Foster, Wolszczan & Camilo (1993), (36) Edwards & Bailes (2001), (37) Janssen et al. (2010), (38) Jacoby (2005), (39) Freire et al. (2012), (40) Kerr et al. (2012), (41) Camilo et al. (2015), (42) Stairs et al. (2005), (43) Faulkner et al. (2004), (44) Lorimer et al. (2006), (45) Ferdman et al. (2010), (46) Lyne et al. (1987), (47) Burgay et al. (2013), (48) Hobbs et al. (2004a), (49) Segelstein et al. (1986), (50) Champion et al. (2008), (51) Freire et al. (2011), (52) Jacoby et al. (2003), (53) Lynch et al. (2013), (54) Backer et al. (1982), (55) Champion et al. (2005), (56) Deneva et al. (2012), (57) Boriakoff, Buccheri & Fauci (1983), (58) Cognard et al. (2011), (59) Nice, Taylor & Fruchter (1993), (60) Nice, Splaver & Stairs (2001), (61) Ray et al. (1996), (62) Ransom et al. (2011), (63) Camilo (1995), and (64) Camilo, Nice & Taylor (1993).

the PPTA data set contains several measured backend-dependent time offsets, which we include as fixed JUMPs in the timing model.

A pulsar timing model generally consists of astrometric parameters (right ascension RA, declination Dec., proper motion in RA and Dec., timing parallax π), rotational frequency information (spin frequency f and its time derivatives), and dispersion measure information (DM; this accounts for the frequency-dependent (FD) time delay of the pulses due to electrons in the interstellar medium along the line of sight). With consistent adequate bandwidth and/or multiple observing frequencies, the time dependence of DM can also be included in the model. If the pulsar is in a binary system, the Keplerian parameters (orbital period P_b, projected semimajor axis x of the pulsar orbit, longitude of periastron ω_0, epoch of periastron passage T_0, and eccentricity e of the orbit) are included to describe its binary motion. Some pulsars also require theory-independent Post-Keplerian parameters (orbital period derivative $\dot{P}_b$, periastron advance $\dot{\omega}_0$, Shapiro delay parameters 'range r' and 'shape s', apparent derivative of the projected semimajor axis $\dot{x}$) to account for any deviation of the orbit from Keplerian motion (see Damour & Deruelle 1985, 1986; Damour & Taylor 1992). A detailed description of all these parameters is given in Lorimer & Kramer (2005). We use the TEMPO2 binary model T2 in general in timing models of binary pulsars. For low-eccentricity pulsars, we use the binary model ELL1 (Wex 1999; Lange et al. 2001), in which the first and second Laplace–Lagrange parameters ($\epsilon_1 = e\sin\omega_0$ and $\epsilon_2 = e\cos\omega_0$) are fitted. For low-eccentricity and medium- to high-inclination binary pulsars, we use the binary model DDH (Freire & Wex 2010) in the timing model in which the amplitude of the third harmonic of the orbital period (H3) and the ratio of amplitudes of successive harmonics (STIG) are fitted.

In the fitting process, the measured topocentric ToAs are converted to the Solar system barycentric coordinate time (TCB) through the Solar system ephemeris DE436[4] using the Terrestrial Time standard BIPM2015.[5] The barycentric dynamical time (TDB) is commonly used in astronomy and thus, we also convert our timing results to TDB units and include the solutions in the data release separately. To develop the timing model for each pulsar, we started by fitting the timing model parameters from one of the individual PTA data releases. We then added any additional parameters needed to accommodate the other individual PTA data releases, and we tested for further parameters that might be needed in the combined data set (as described below).

If the pulsar is observed by NANOGrav, we then include 'FD' parameters in the timing model because of the availability of the FD sub-band ToAs to minimize the effect of FD pulse profile evolution (Arzoumanian et al. 2015b). The number of required FD parameters for a given pulsar is obtained from Arzoumanian et al. (2015b).

To model the white noise σ (uncorrelated in time) of the pulsar data, we include the standard noise parameters EFAC (E_f) and EQUAD (E_q) for each data set in the timing model (see Verbiest

[4]This Solar system ephemeris is based on Folkner et al. (2014).

[5]This time standard has been obtained according to principles given in Guinot (1988) and Petit (2003).

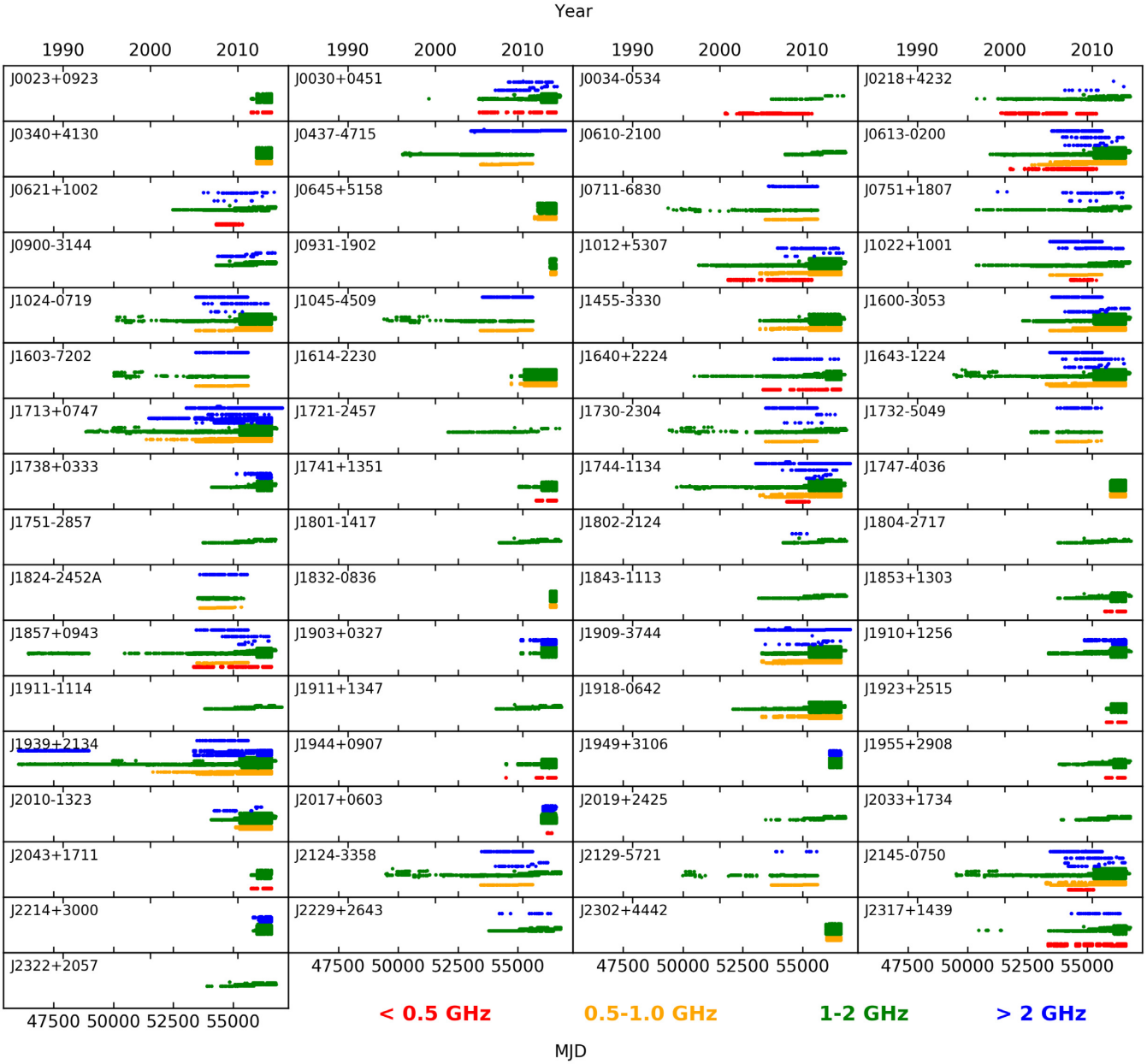

Figure 2. The frequency coverage and the time baseline of the observations used in IPTA dr2 for each pulsar. Note that all pulsars are observed at *L* band (∼1400 MHz). The *y*-axis of each panel represents a frequency range of approximately 0–4 GHz in linear scale. The frequency of each ToA is plotted, so that approximately the entire bandwidth is shown for NANOGrav observations because of their available sub-band ToAs.

et al. 2016, for details). The EFAC is a scale parameter on the ToA uncertainty and the EQUAD is an added variance that mainly accounts for the error caused by pulse phase-jitter (Osłowski et al. 2011, 2013) and other systematic effects. The TEMPO2 version (Edwards et al. 2006) defines the relationship of these two parameters to a ToA uncertainty σ_t as

$$\sigma = E_f \sqrt{E_q^2 + \sigma_t^2}, \quad (1)$$

while the TEMPONEST version (Lentati et al. 2014) defines the relationship in a reverse order as

$$\sigma = \sqrt{E_q^2 + E_f^2 \sigma_t^2}. \quad (2)$$

TEMPONEST[6] is a pulsar noise analysis plugin in TEMPO2 that is based on Bayesian analysis (Lentati et al. 2014). We also include the factor ECORR to correct for the pulse phase jitter that causes correlation between simultaneous ToAs obtained at different observing frequencies. In the data combination, we include separate EFACs and EQUADs for all telescope/backend-dependent PTA data sets, and separate ECORRs for telescope/backend-dependent NANOGrav data sets because of their available simultaneous FD ToAs (i.e. sub-band ToAs).

In addition to white noise, we model the time-correlated red noise processes by including the stochastic DM variation and the

[6] https://github.com/LindleyLentati/TempoNest

spin noise processes with power-law models in the timing solution. We use the TEMPONEST plugin to determine the white and red noise parameters by fitting simultaneously while marginalizing over the timing model parameters (see Lentati et al. 2014, for more details of the software). We note that, as shown in Lentati et al. (2016), some pulsars in the IPTA dr1 needed additional red noise processes such as 'system noise' and 'band noise' to accurately model the noise in their timing data. The system noise models possible instrumental effects and calibration errors that might appear in a single observing system or telescope. The band noise models signals that exist in a given frequency band. These signals may have originated in the interstellar medium due to processes that are incoherent between different bands, or that do not scale in amplitude with the inverse square of the observing frequency, or due to radio frequency interference that present in the same band independent of the observing site. Therefore, our basic DM and spin noise processes may not provide the optimal model. A detailed noise analysis will be carried out separately in a future study.

The individual PTA data releases used different methods of modelling DM variations: the EPTA data release used the first two time derivatives of the DM and the stochastic DM variation with a power law (Caballero et al. 2016; Desvignes et al. 2016); the PPTA data release used only the first two time derivatives of the DM (Reardon et al. 2016); and the NANOGrav data release measured the change in DM, relative to the fiducial DM value in the timing model, at nearly every observing epoch using the TEMPO[7] 'DMX' parameter (Arzoumanian et al. 2015b). In this IPTA data combination, we use two different methods to model the DM variation, including the model DMMODEL given in Keith et al. (2013) as described in Section 4.1, and time derivatives of the DM with a power-law stochastic DM variation as described in Section 4.2.

Finally, with the fully combined data set and timing model for each pulsar, we use an F-test with the residual sum of squares of each model, as described in Arzoumanian et al. (2015b), to search for parameters that have become significant as a result of combining the data. This process is used in all NANOGrav data releases to ensure the model is as complete as possible. With the addition of a new parameter, an F-test significance value of $\leq$0.0027 (i.e. 3σ significance) implies that the additional parameter has significantly improved the model's description of the data. For long data sets, the most likely parameters to become significant are post-Keplerian parameters; additionally, the use of wide-bandwidth or multiband data may require higher order 'FD' parameters to model FD pulse shape evolution, as described in Arzoumanian et al. (2015b). After having combined the timing models as described earlier in this section, with this F-test analysis we do not find any additional parameters that are required in IPTA dr2 pulsar timing models beyond those used in the individual PTA data sets.

4 RESULTS

We produce two data combination versions (VersionA and VersionB) in the IPTA dr2 and the data set is available at http://www.ipta4gw.org. We also note that the data set includes separate timing solutions for pulsars produced with TCB and TDB units. The two versions are different in terms of modelling the DM variation and handling the noise properties of pulsars, and they are described below in detail.

[7]http://tempo.sourceforge.net/

4.1 IPTA dr2 – VersionA

In this version, we determine the DM variation using the model given in Keith et al. (2013) and implemented in TEMPO2 as DMMODEL. This model estimates the DM offsets from the global value as a function of time for a given time grid. We use a 60 d MJD grid in general for all pulsars in the combination, but a 30 d grid is used for several sources to better constrain DM variations. For pulsars with a lack of multifrequency observations (or a shorter time span of multifrequency coverage), the DMMODEL does not provide reliable results and thus, we use the basic time derivatives of the DM (i.e. $\dot{\mathrm{DM}}$ and $\ddot{\mathrm{DM}}$) in the timing model (see the ninth column in Table 2). We include only white noise parameters EFACs and EQUADs in the timing model of pulsars in this version. Note that we do not constrain them using this IPTA data combination, rather we use the values constrained in previous data releases. The EFACs and EQUADs for the EPTA data are taken from the EPTA dr1 (Desvignes et al. 2016), those for the PPTA data are taken from the IPTA dr1 (Verbiest et al. 2016). These EPTA and PPTA white noise parameters were constrained using TEMPONEST according to the ToA uncertainty scaling given in equation (2). For NANOGrav data, we use the TEMPO2 version of EFACs and EQUADs (see equation 1), which are taken from the NANOGrav data release (Arzoumanian et al. 2015b). Finally we update timing models of all 65 pulsars by running TEMPO2 using the combined IPTA data set.

Fig. 3 shows the time-dependent DM variation obtained from DMMODEL for pulsars that are observed by all three PTAs. Note that we did not include PSR J1939+2134 in Fig. 3 because of its complicated DM variation and timing noise (e.g. Kaspi et al. 1994; Manchester et al. 2013; Arzoumanian et al. 2015b; Caballero et al. 2016; Desvignes et al. 2016; Lentati et al. 2016). These results are consistent with the DM variations of pulsars presented in Keith et al. (2013) using the PPTA data, and also with the results obtained using the DMX method that are presented in Arzoumanian et al. (2015b) using the NANOGrav data.

4.2 IPTA dr2 – VersionB

The main difference of this version compared to VersionA is in the modelling of the white and red noise processes and DM variations of the pulsars. We re-estimate all the noise parameters of pulsars based on this IPTA data combination, rather than using previously constrained values given in other data releases. We include new EFACs and EQUADs for all PTA data sets and separate ECORRs for NANOGrav data sets if available in the pulsar timing model. We include the first two time derivatives of the DM and then model the time-correlated stochastic DM and the red spin noise processes using separate power-law models in the timing model. Using TEMPONEST, we then constrain these noise parameters simultaneously while marginalizing over the timing model parameters. For comparison with VersionA, we overplot the DM variations for pulsars that are observed by all three PTAs in Fig. 3. This shows that the overall time-dependent DM variations modelled by these two methods are largely consistent with each other within their uncertainties.

We present the timing residuals of pulsars in Figs 4 and 5. We have subtracted the power-law waveform of the DM stochastic noise in these residuals, but not the waveforms of red spin noise processes. Some pulsars exhibit complicated noise processes and need a more sophisticated noise analysis including various additional noise terms such as systematic noise and band noise as discussed in Lentati et al. (2016). This will be done separately combining with GW search

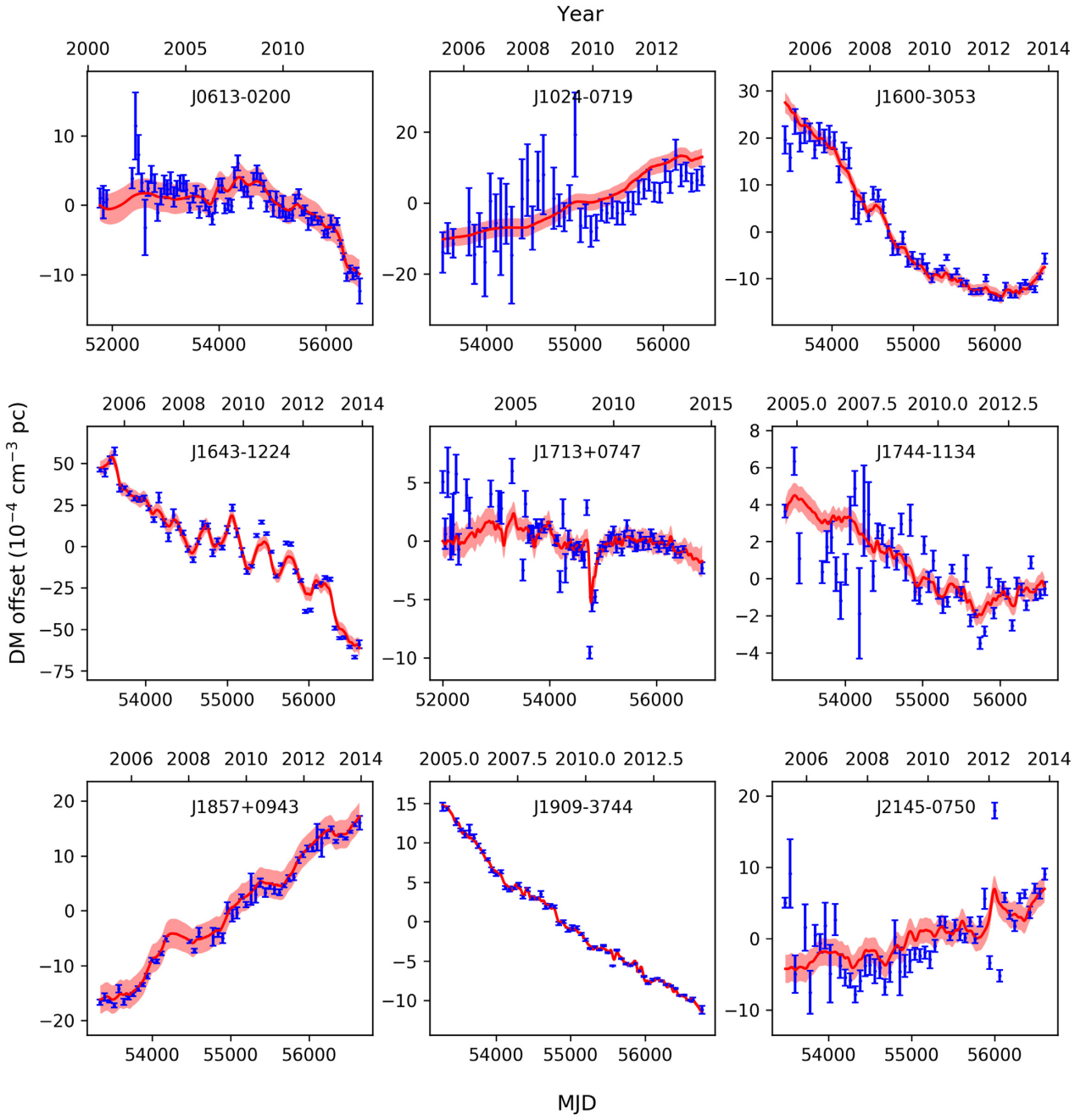

Figure 3. The time-dependent DM variations for pulsars that are observed by all three PTAs obtained using the DMMODEL (*blue*) as described in VersionA (see Section 4.1). Note that the mean DM is subtracted and only the variation is plotted. For comparison, the DM variations obtained using the power-law model described in VersionB (see Section 4.2) are overplotted (*red*), and their uncertainties are estimated using a Gaussian process regression method. The overall features in DM variations obtained from the two versions are consistent with each other within their measured uncertainties. Note that we omitted PSR J1939+2134 in this figure because of its complicated timing noise behaviour.

analyses using this new data combination in the future. We present the best timing models for all our pulsars in Appendix A.

5 DISCUSSION

In this paper, we presented the creation of the IPTA second data release (IPTA dr2) that includes the EPTA, NANOGrav, and PPTA data releases presented in Desvignes et al. (2016), Arzoumanian et al. (2015b), and Reardon et al. (2016), respectively. This new IPTA data release consists of regularly observed high-precision timing data of 65 MSPs, which includes 16 additional MSPs compared to the previous IPTA dr1. We produced two versions in the data release (i.e. VersionA and VersionB) depending on different methods of handling the DM and the noise processes of pulsars as described in Section 4. We directly compared the timing ephemerides of pulsars obtained from the two versions in this new IPTA dr2 and the previous IPTA dr1. We found that all

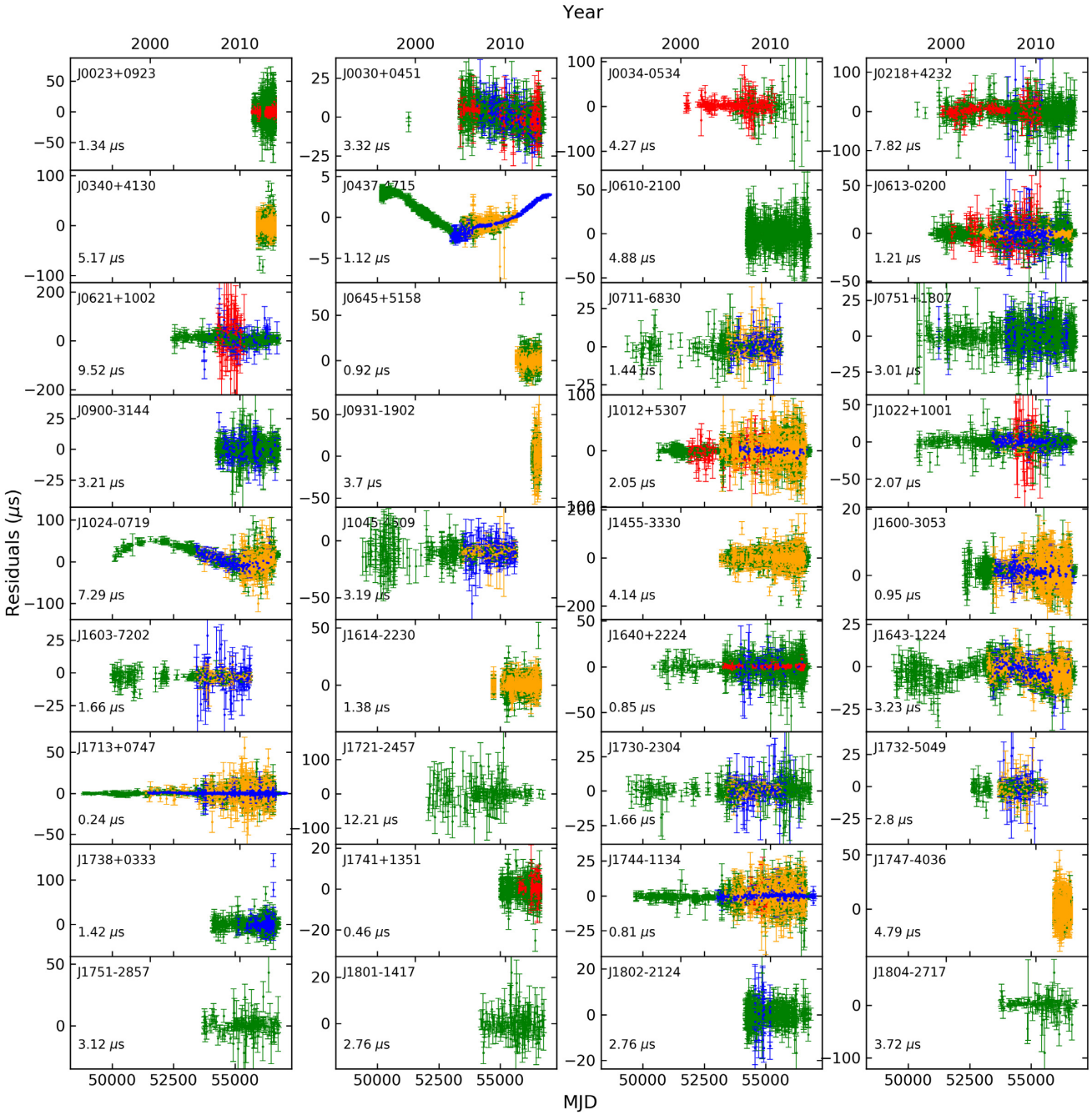

Figure 4. The timing residuals (i.e. the difference between the observed and timing model predicted ToAs) of the first 36 pulsars obtained using the data combination VersionB (see Section 4.2). The maximum-likelihood waveform of the power-law stochastic DM variation model is subtracted from the residuals, but the red spin noise model has not been subtracted. The pulsar name is given in the top and the weighted root-mean-square of the timing residuals is given in the bottom of each panel. The colour code represents different observing frequencies as given in Fig. 2: <0.5 GHz (red), 0.5–1.0 GHz (orange), 1–2 GHz (green), and >2 GHz (blue).

the timing parameters are greatly consistent with each other and their uncertainties resulted in IPTA dr2 are generally improved compared to the IPTA dr1, mostly due to the addition of more data in the combination. We also compared the DM variations of pulsars obtained using VersionA and VersionB (see Fig. 3). This comparison shows that the overall features in the variations are consistent with each other within their uncertainties, including the uncertainty of the mean DM measurement in the timing model. We note that the DMMODEL provides much noisier variation compared to the power-law model. This is because the DMMODEL follows a piecewise method using a given time-grid, which depends on observation sampling and the availability of multifrequency data (see Keith et al. 2013). In contrast, the power-law model fits for the power spectrum of the timing data and the waveform of the DM variation can be generated for any given time series (see Lee et al. 2014; Lentati et al. 2014)

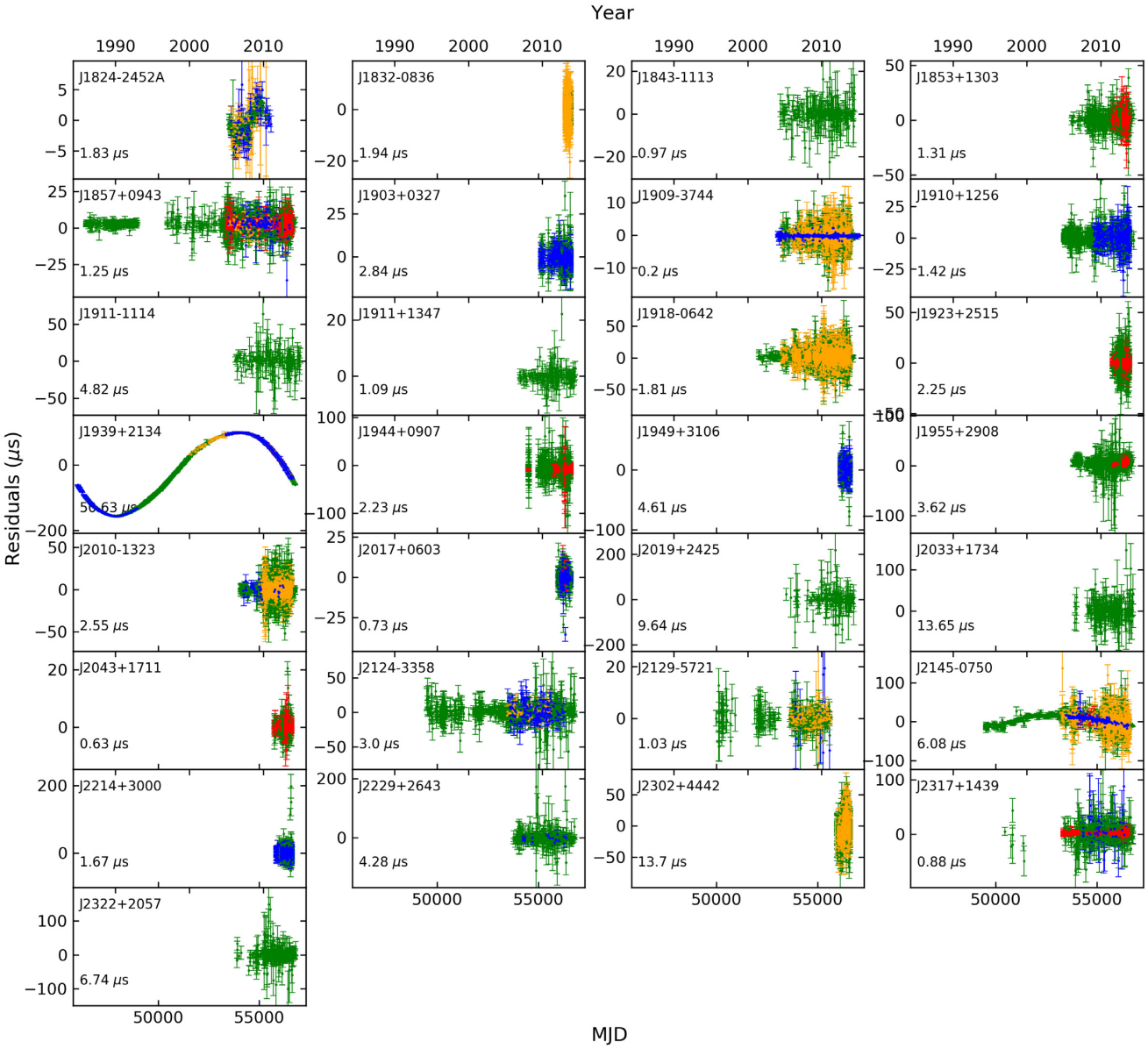

Figure 5. Same as Fig. 4, but for the last 29 pulsars.

We only constrained the basic noise properties of pulsars in this data combination. However, using IPTA dr1, Lentati et al. (2016) showed that some pulsars need additional noise terms such as system and band noise to model their overall noise properties accurately because of the involvement of several observing systems (i.e. backends/telescopes) in the observations and also wider frequency coverages. By simply comparing the weighted root mean square (rms) of timing residuals after subtracting the maximum-likelihood time-correlated noise signals (i.e. by comparing σ_w in Table 2 herein and table 1 in Lentati et al. 2016), we found that approximately 60 per cent of pulsars have improved their timing precision based on this new IPTA dr2 compared to the previous IPTA dr1. The rest of the pulsars have slightly poorer timing precision compared to the previous data release, probably because these pulsars require additional noise terms to optimize their noise analysis as described in Lentati et al. (2016) which we have ignored in the present analysis. Thus, a detailed noise modelling based on the IPTA dr2 will be required and conducted in subsequent analysis. This will be published separately in the future.

Adding new data is essential to improve the timing precision and the sensitivity of the IPTA to GWs. We also need to consider and understand these new data and their noise behaviour to be able to achieve optimal results. This requires additional noise investigation and more computationally expensive methods to model their noise behaviours, which can be very time consuming. For instance, the data sets of PSRs J1713+0747 and J1939+2134 in the IPTA dr2 are long and dense due to the involvement of all IPTA telescopes in the observations with several backends providing broad frequency coverage. Based on our basic noise analysis, J1713+0747 and J1939+2134 required 90 and 74 noise parameters, respectively, in the timing model requiring weeks of computer time to conduct their noise analyses. We will have more pulsar data available for

the IPTA in the future and their noise analyses will become even more complicated. Therefore, we need to investigate methods to improve the efficiencies of current pulsar noise analysis software and also novel techniques to constrain noise in more efficient ways. While we have assumed here that all stochastic processes have power-law spectra, in the future it may be necessary to consider more complex models to be able to understand the pulsar noise behaviours more accurately. This will become important especially when high-resolution data are available for the IPTA from modern telescopes such as MeerKAT and Square Kilometre Array, and also with the instrument upgrades of current telescopes in the IPTA.

6 FUTURE IPTA STUDIES

The primary goal of the IPTA is to detect and characterize low-frequency GWs using high-precision pulsar timing (Verbiest et al. 2016). The IPTA dr2 is the most complete MSP data set produced up-to-date for GW search experiments. There are a suite of papers which are currently exploring the broader impacts of IPTA dr2. In terms of GW search analyses, we are preparing improved GW background constraints that revise upper limits from Shannon et al. (2015) and Lentati et al. (2015) by accounting for Solar system effects using BAYESEPHEM (Arzoumanian et al. 2018b), and will apply more flexible DM variation models to Arzoumanian et al. (2015b). We are exploring the detection response of the IPTA to the GW background, and how this compares to that of the constituent regional PTA data sets. We are also carrying out a search for GW memory (Braginskii & Thorne 1987; van Haasteren & Levin 2010; Wang et al. 2015; Arzoumanian et al. 2015a; Madison, Chernoff & Cordes 2017), in addition to exploring new and novel ways of analyzing IPTA data. These include (but are not limited to) the identification and removal of legacy ToAs which do not contribute to our GW background sensitivity, as well as the preparation of smaller IPTA data sets that require minimal combination efforts from the constitutent PTAs, thereby enabling fast diagnostics. Potential avenues of future GW study with this data include searching for individually resolvable supermassive black hole binary systems (Zhu et al. 2014; Babak et al. 2016; Aggarwal et al. 2018), and placing constraints on beyond-General-Relativity GW polarization states (Lee, Jenet & Price 2008; Lee et al. 2010; Chamberlin & Siemens 2012; Lee 2013; Gair, Romano & Taylor 2015; Cornish et al. 2018; O'Beirne et al. 2019).

We expect IPTA dr2 to also impact many areas that are synergistic to nanohertz GW searches, including (but not limited to): probing ultralight scalar-field dark matter (the so-called 'fuzzy' dark matter) in the particle mass range 10^{-24}–10^{-22} eV (Porayko et al. 2018, and references therein); improving the characterization of radio-frequency–dependent delay processes induced by the ionized interstellar medium (Keith et al. 2013; Jones et al. 2017; Lam et al. 2017) and solar wind (Niu et al. 2017; Madison et al. 2019; Tiburzi et al. 2019); studying the Solar system and giving independent constraints on ephemeris parameters with pulsar-timing data (Caballero et al. 2018; Guo, Lee & Caballero 2018; Arzoumanian et al. 2018b); and synthesizing a pulsar-based time standard (Hobbs et al. 2012). Several of these goals (both GW and synergistic) may be aided by improved pulsar distance precision and discovery techniques (e.g. Jennings et al. 2018; Mingarelli et al. 2018; Deller et al. 2019).

ACKNOWLEDGEMENTS

The National Radio Astronomy Observatory is a facility of the National Science Foundation operated under cooperative agreement by Associated Universities, Inc. The NANOGrav Physics Frontiers Center is supported by NSF award number 1430284. The Green Bank Observatory is a facility of the National Science Foundation operated under cooperative agreement by Associated Universities, Inc. The Arecibo Observatory is operated by the University of Central Florida, Ana G. Mendez-Universidad Metropolitana, and Yang Enterprises under a cooperative agreement with the National Science Foundation (NSF; AST-1744119). The Parkes telescope is part of the Australia Telescope which is funded by the Commonwealth Government for operation as a National Facility managed by CSIRO. The Westerbork Synthesis Radio Telescope is operated by the Netherlands Institute for Radio Astronomy (ASTRON) with support from The Netherlands Foundation for Scientific Research NWO. The 100-m Effelsberg Radio Telescope is operated by the Max-Planck-Institut für Radioastronomie at Effelsberg. Some of the work reported in this paper was supported by the ERC Advanced Grant 'LEAP', Grant Agreement Number 227947 (PI Kramer). Pulsar research at the Jodrell Bank Centre for Astrophysics is supported by a consolidated grant from STFC. The Nancay radio telescope is operated by the Paris Observatory, associated with the Centre National de la Recherche Scientifique (CNRS) and acknowledges financial support from the 'Programme National de Cosmologie et Galaxies (PNCG)' and 'Gravitation, Références, Astronomie, Métrologie (GRAM)' programmes of CNRS/INSU, France. The Flatiron Institute is supported by the Simons Foundation. This work was supported by the NANOGrav Physics Frontiers Center (NSF award 1430284). Parts of this research were conducted by the Australian Research Council Centre of Excellence for Gravitational Wave Discovery (OzGrav), through project number CE170100004. SO and RS acknowledge Australian Research Council grant FL150100148. SMR is a CIFAR Fellow. GD and KL acknowledges financial support by the European Research Council for the ERC Synergy Grant BlackHoleCam under contract no. 610058. KJL is supported by XDB23010200, NSFC U15311243, 2017YFA0402600 and funding from TianShanChuangXinTuanDui and Max-Planck Partner Group. MAM and SBS are supported by NSF award number 1458952. JBW is supported by the Youth Innovation Promotion Association of Chinese Academy of Sciences. WWZ is supported by Chinese Academy of Science Pioneer Hundred Talents Program, the Strategic Priority Research Program of the Chinese Academy of Sciences Grant No. XDB23000000, and by the National Natural Science Foundation of China under grant No. 11743002, 11873067. Part of this research was performed at the Jet Propulsion Laboratory, under contract with the National Aeronautics and Space Administration. JS and MV acknowledges support from the JPL R&TD program. Basic pulsar research at NRL is funded by the Chief of Naval Research. Pulsar research at UBC is supported by an NSERC Discovery Grant and by the Canadian Institute for Advanced Research.

REFERENCES

Abdo A. A. et al., 2010, ApJ, 712, 957
Aggarwal K. et al., 2019, ApJ, 880, 116
Alpar M. A., Cheng A. F., Ruderman M. A., Shaham J., 1982, Nature, 300, 728
Arzoumanian Z. et al., 2014, ApJ, 794, 141
Arzoumanian Z. et al., 2015a, ApJ, 810, 150
Arzoumanian Z. et al., 2015b, ApJ, 813, 65
Arzoumanian Z. et al., 2016, ApJ, 821, 13
Arzoumanian Z. et al., 2018a, ApJS, 235, 37
Arzoumanian Z. et al., 2018b, ApJ, 859, 47
Babak S. et al., 2016, MNRAS, 455, 1665

Backer D. C., Kulkarni S. R., Heiles C., Davis M. M., Goss W. M., 1982, Nature, 300, 615
Bailes M. et al., 1994, ApJ, 425, L41
Bailes M. et al., 1997, ApJ, 481, 386
Boriakoff V., Buccheri R., Fauci F., 1983, Nature, 304, 417
Braginskii V. B., Thorne K. S., 1987, Nature, 327, 123
Burgay M. et al., 2006, MNRAS, 368, 283
Burgay M. et al., 2013, MNRAS, 433, 259
Caballero R. N. et al., 2016, MNRAS, 457, 4421
Caballero R. N. et al., 2018, MNRAS, 481, 5501
Camilo F., 1995, PhD thesis, Princeton Univ.
Camilo F., Nice D. J., Taylor J. H., 1993, ApJ, 412, L37
Camilo F., Nice D. J., Shrauner J. A., Taylor J. H., 1996, ApJ, 469, 819
Camilo F. et al., 2015, ApJ, 810, 85
Chamberlin S. J., Siemens X., 2012, Phys. Rev. D, 85, 082001
Champion D. J. et al., 2005, MNRAS, 363, 929
Champion D. J. et al., 2008, Science, 320, 1309
Cognard I. et al., 2011, ApJ, 732, 47
Corbin V., Cornish N. J., 2010, preprint(arXiv:1008.1782)
Cornish N. J., O'Beirne L., Taylor S. R., Yunes N., 2018, Phys. Rev. Lett., 120, 181101
Crawford F., Roberts M. S. E., Hessels J. W. T., Ransom S. M., Livingstone M., Tam C. R., Kaspi V. M., 2006, ApJ, 652, 1499
Damour T., Deruelle N., 1985, Ann. Inst. Henri Poincaré Phys. Théor, 43, 107
Damour T., Deruelle N., 1986, Ann. Inst. Henri Poincaré Phys. Théor, 44, 263
Damour T., Taylor J. H., 1992, Phys. Rev. D, 45, 1840
Deller A. T., Verbiest J. P. W., Tingay S. J., Bailes M., 2008, ApJ, 685, L67
Deller A. T. et al., 2019, ApJ, 875, 100
Deneva J. S. et al., 2012, ApJ, 757, 89
Desvignes G. et al., 2016, MNRAS, 458, 3341
Detweiler S., 1979, ApJ, 234, 1100
Du Y., Yang J., Campbell R. M., Janssen G., Stappers B., Chen D., 2014, ApJ, 782, L38
Edwards R. T., Bailes M., 2001, ApJ, 553, 801
Edwards R. T., Hobbs G. B., Manchester R. N., 2006, MNRAS, 372, 1549
Ellis J. A., 2013, Class. Quantum Gravity, 30, 224004
Faulkner A. J. et al., 2004, MNRAS, 355, 147
Ferdman R. D. et al., 2010, ApJ, 711, 764
Folkner W. M., Williams J. G., Boggs D. H., Park R. S., Kuchynka P., 2014, Interplanetary Network Progress Report, 196, 1
Foster R. S., Wolszczan A., Camilo F., 1993, ApJ, 410, L91
Freire P. C. C., Wex N., 2010, MNRAS, 409, 199
Freire P. C. C. et al., 2011, MNRAS, 412, 2763
Freire P. C. C. et al., 2012, MNRAS, 423, 3328
Gaia Collaboration, 2018, A&A, 616, A1
Gair J. R., Romano J. D., Taylor S. R., 2015, Phys. Rev. D, 92, 102003
Goldstein J. M., Veitch J., Sesana A., Vecchio A., 2018, MNRAS, 477, 5447
Guillemot L. et al., 2016, A&A, 587, A109
Guinot B., 1988, A&A, 192, 370
Guo Y. J., Lee K. J., Caballero R. N., 2018, MNRAS, 475, 3644
Hellings R. W., Downs G. S., 1983, ApJ, 265, L39
Hessels J. W. T. et al., 2011, in Burgay M., D'Amico N., Esposito P., Pellizzoni A., Possenti A., eds, AIP Conf. Proc. Vol. 1357, Radio Pulsars: An Astrophysical Key to Unlock the Secrets of the Universe. Am. Inst. Phys., New York, p. 40
Hobbs G. et al., 2004a, MNRAS, 352, 1439
Hobbs G., Lyne A. G., Kramer M., Martin C. E., Jordan C., 2004b, MNRAS, 353, 1311
Hobbs G. B., Edwards R. T., Manchester R. N., 2006, MNRAS, 369, 655
Hobbs G. et al., 2012, MNRAS, 427, 2780
Hotan A. W., Bailes M., Ord S. M., 2006, MNRAS, 369, 1502
Jacoby B. A., 2005, PhD thesis, California Institute of Technology
Jacoby B. A., Bailes M., van Kerkwijk M. H., Ord S., Hotan A., Kulkarni S. R., Anderson S. B., 2003, ApJ, 599, L99
Jacoby B. A., Bailes M., Ord S. M., Knight H. S., Hotan A. W., 2007, ApJ, 656, 408
Jankowski F., van Straten W., Keane E. F., Bailes M., Barr E. D., Johnston S., Kerr M., 2018, MNRAS, 473, 4436
Janssen G. H., Stappers B. W., Bassa C. G., Cognard I., Kramer M., Theureau G., 2010, A&A, 514, A74
Jenet F. A., Hobbs G. B., Lee K. J., Manchester R. N., 2005, ApJ, 625, L123
Jennings R. J., Kaplan D. L., Chatterjee S., Cordes J. M., Deller A. T., 2018, ApJ, 864, 26
Johnston S. et al., 1993, Nature, 361, 613
Jones M. L. et al., 2017, ApJ, 841, 125
Kaspi V. M., Taylor J. H., Ryba M. F., 1994, ApJ, 428, 713
Keith M. J. et al., 2013, MNRAS, 429, 2161
Kelley L. Z., Blecha L., Hernquist L., Sesana A., Taylor S. R., 2017, MNRAS, 471, 4508
Kelley L. Z., Blecha L., Hernquist L., Sesana A., Taylor S. R., 2018, MNRAS, 477, 964
Kerr M. et al., 2012, ApJ, 748, L2
Kramer M., Xilouris K. M., Lorimer D. R., Doroshenko O., Jessner A., Wielebinski R., Wolszczan A., Camilo F., 1998, ApJ, 501, 270
Lam M. T. et al., 2017, ApJ, 834, 35
Lange C., Camilo F., Wex N., Kramer M., Backer D. C., Lyne A. G., Doroshenko O., 2001, MNRAS, 326, 274
Lazaridis K. et al., 2009, MNRAS, 400, 805
Lee K., Jenet F. A., Price R. H., Wex N., Kramer M., 2010, ApJ, 722, 1589
Lee K. J., 2013, Class. Quantum Gravity, 30, 224016
Lee K. J., Jenet F. A., Price R. H., 2008, ApJ, 685, 1304
Lee K. J., Wex N., Kramer M., Stappers B. W., Bassa C. G., Janssen G. H., Karuppusamy R., Smits R., 2011, MNRAS, 414, 3251
Lee K. J. et al., 2014, MNRAS, 441, 2831
Lentati L., Alexander P., Hobson M. P., Feroz F., van Haasteren R., Lee K. J., Shannon R. M., 2014, MNRAS, 437, 3004
Lentati L. et al., 2015, MNRAS, 453, 2576
Lentati L. et al., 2016, MNRAS, 458, 2161
Levin L. et al., 2016, ApJ, 818, 166
Lommen A. N., Zepka A., Backer D. C., McLaughlin M., Cordes J. M., Arzoumanian Z., Xilouris K., 2000, ApJ, 545, 1007
Lorimer D. R., Kramer M., 2005, Handbook of Pulsar Astronomy. Cambridge Univ. Press, Cambridge
Lorimer D. R. et al., 1995, ApJ, 439, 933
Lorimer D. R., Lyne A. G., Bailes M., Manchester R. N., D'Amico N., Stappers B. W., Johnston S., Camilo F., 1996, MNRAS, 283, 1383
Lorimer D. R. et al., 2006, MNRAS, 372, 777
Lundgren S. C., Zepka A. F., Cordes J. M., 1995, ApJ, 453, 419
Lynch R. S. et al., 2013, ApJ, 763, 81
Lyne A. G., Brinklow A., Middleditch J., Kulkarni S. R., Backer D. C., Clifton T. R., 1987, New Astron., 328, 399
Madison D. R., Chernoff D. F., Cordes J. M., 2017, Phys. Rev. D, 96, 123016
Madison D. R. et al., 2019, ApJ, 872, 150
Manchester R. N. et al., 2013, Publ. Astron. Soc. Aust., 30, e017
Mingarelli C. M. F., Grover K., Sidery T., Smith R. J. E., Vecchio A., 2012, Phys. Rev. Lett., 109, 081104
Mingarelli C. M. F. et al., 2017, Nat. Astron., 1, 886
Mingarelli C. M. F., Anderson L., Bedell M., Spergel D. N., 2018, preprint(arXiv:1812.06262)
Navarro J., de Bruyn G., Frail D., Kulkarni S. R., Lyne A. G., 1995, ApJ, 455, L55
Nicastro L., Lyne A. G., Lorimer D. R., Harrison P. A., Bailes M., Skidmore B. D., 1995, MNRAS, 273, L68
Nice D. J., Taylor J. H., Fruchter A. S., 1993, ApJ, 402, L49
Nice D. J., Splaver E. M., Stairs I. H., 2001, ApJ, 549, 516
Niu Z.-X., Hobbs G., Wang J.-B., Dai S., 2017, Res. Astron. Astrophys., 17, 103
O'Beirne L., Cornish N. J., Vigeland S. J., Taylor S. R., 2019, Phys. Rev. D, 99, 124039
Osłowski S., van Straten W., Hobbs G. B., Bailes M., Demorest P., 2011, MNRAS, 418, 1258

Osłowski S., van Straten W., Demorest P., Bailes M., 2013, MNRAS, 430, 416
Perera B. B. P. et al., 2018, MNRAS, 478, 218
Petit G., 2003, 35th Annual Precise Time and Time Interval (PTTI) Meeting. San Diego, p. 307
Porayko N. K. et al., 2018, Phys. Rev. D, 98, 102002
Radhakrishnan V., Srinivasan G., 1982, Curr. Sci., 51, 1096
Ransom S. M. et al., 2011, ApJ, 727, L16
Ray P. S., Thorsett S. E., Jenet F. A., van Kerkwijk M. H., Kulkarni S. R., Prince T. A., Sandhu J. S., Nice D. J., 1996, ApJ, 470, 1103
Reardon D. J. et al., 2016, MNRAS, 455, 1751
Rosado P. A., Sesana A., Gair J., 2015, MNRAS, 451, 2417
Segelstein D. J., Rawley L. A., Stinebring D. R., Fruchter A. S., Taylor J. H., 1986, Nature, 322, 714
Sesana A., Vecchio A., 2010, Phys. Rev. D, 81, 104008
Shannon R. M. et al., 2015, Science, 349, 1522
Siemens X., Ellis J., Jenet F., Romano J. D., 2013, Class. Quantum Gravity, 30, 224015
Stairs I. H. et al., 2005, ApJ, 632, 1060
Stovall K. et al., 2014, ApJ, 791, 67
Taylor S., Ellis J., Gair J., 2014, Phys. Rev. D, 90, 104028
Taylor S. R., Vallisneri M., Ellis J. A., Mingarelli C. M. F., Lazio T. J. W., van Haasteren R., 2016, ApJ, 819, L6
Tiburzi C. et al., 2019, MNRAS, 487, 394
Toscano M., Bailes M., Manchester R., Sandhu J., 1998, ApJ, 506, 863
van Haasteren R., Levin Y., 2010, MNRAS, 401, 2372
Verbiest J. P. W. et al., 2008, ApJ, 679, 675
Verbiest J. P. W. et al., 2009, MNRAS, 400, 951
Verbiest J. P. W., Weisberg J. M., Chael A. A., Lee K. J., Lorimer D. R., 2012, ApJ, 755, 39
Verbiest J. P. W. et al., 2016, MNRAS, 458, 1267
Wang J. B. et al., 2015, MNRAS, 446, 1657
Wex N., 1999, Implementation of Laplace-Lagrange Parameters in TEMPO. Private communication
Yao J. M., Manchester R. N., Wang N., 2017, ApJ, 835, 29
Yardley D. R. B. et al., 2010, MNRAS, 407, 669
Zhu X.-J. et al., 2014, MNRAS, 444, 3709
Zhu X.-J., Wen L., Xiong J., Xu Y., Wang Y., Mohanty S. D., Hobbs G., Manchester R. N., 2016, MNRAS, 461, 1317
Zhu W. W. et al., 2015, ApJ, 809, 41

APPENDIX A: TIMING MODELS

In this appendix, we present the updated timing solutions for all 65 MSPs (see Table A1) according to VersionB as described in Section 4.2 based on this most up-to-date IPTA data combination.

Table A1. Timing solutions of pulsars based on VersionB described in Section 4.2. The values in parentheses represent the 1σ uncertainty of the last displayed digit for the parameter. The description of parameters is given in Section 3.

	J0023+0923	J0030+0451	J0034−0534	J0218+4232
MJD range	55757−56600	51275−56780	51769−56707	50370−56788
Number of ToAs	4373	3362	276	1196
Weighted rms timing residual (μs)	1.34	3.32	4.27	7.82
Reduced χ^2	1.01	1.01	0.93	1.02
Reference epoch	56200	55000	55000	55000
Units	TCB	TCB	TCB	TCB
Right ascension, RA (J2000)	00:23:16.87910(2)	00:30:27.42838(3)	00:34:21.83424(8)	02:18:06.35731(2)
Declination, Dec. (J2000)	+09:23:23.8689(8)	+04:51:39.707(1)	−05:34:36.722(3)	+42:32:17.3821(4)
Proper motion in RA (mas yr^{-1})	−12.4(5)	−6.4(1)	7.9(3)	5.31(8)
Proper motion in Dec. (mas yr^{-1})	−6.1(10)	0.9(3)	−9.2(6)	−3.1(1)
Spin frequency, f (s^{-1})	327.847 015 546 207(3)	205.530 695 938 454(2)	532.713 429 395 22(3)	430.461 054 545 75(2)
$\dot{f}$ (s^{-2})	$-1.2281(4) \times 10^{-15}$	$-4.2977(2) \times 10^{-16}$	$-1.4127(3) \times 10^{-15}$	$-1.43412(1)^{-14}$
Parallax, π (mas)	0.4(3)	2.94(9)	–	–
Dispersion measure, DM (cm^{-3} pc)	14.328 28(7)	4.332 93(5)	13.765(2)	61.248(2)
$\dot{\mathrm{DM}}$ (cm^{-3} pc yr^{-1})	$1(2) \times 10^{-5}$	$1.0(4) \times 10^{-5}$	$-1.4(10) \times 10^{-4}$	$-3(5) \times 10^{-4}$
$\ddot{\mathrm{DM}}$ (cm^{-3} pc yr^{-2})	$-1.7(6) \times 10^{-4}$	$-4(1) \times 10^{-6}$	$-3(1) \times 10^{-5}$	$6(5) \times 10^{-5}$
Binary model	ELL1	–	T2	T2
Orbital period, P_b (d)	0.138 799 144 63(4)	–	1.589 281 8253(2)	2.028 846 115 60(9)
Epoch of periastron, T_0 (MJD)	56178.836(4)	–	54238.87(4)	53577.82(2)
Projected semimajor axis, x (lt-s)	0.0348410(1)	–	1.4377662(5)	1.9844344(4)
Longitude of periastron, ω_0 (deg)	81(11)	–	312(9)	48(3)
Eccentricity, e	$2.5(5) \times 10^{-5}$	–	$4.4(7) \times 10^{-6}$	$6.8(4) \times 10 - 6$
Epoch of ascending node, T_asc (MJD)	56178.80509387(8)	–	54237.4968265(1)	53577.55114132(7)
$\epsilon_1 = e\sin\omega_0$	$2.4(5) \times 10^{-5}$	–	$-3.3(7) \times 10^{-6}$	$5.1(4) \times 10^{-6}$
$\epsilon_2 = e\cos\omega_0$	$4(5) \times 10^{-6}$	–	$2.9(6) \times 10^{-6}$	$4.6(4) \times 10^{-6}$
	J0340+4130	J0437−4715	J0610−2100	J0613−0200
MJD range	55971−56587	50191−56978	54269−56793	50931−56797
Number of ToAs	3003	5302	1034	9322
Weighted rms timing residual (μs)	5.17	1.12	4.88	1.21
Reduced χ^2	1.00	1.01	0.98	0.89
Reference epoch	56279	55000	55000	55000
Units	TCB	TCB	TCB	TCB
Right ascension, RA (J2000)	03:40:23.28822(1)	04:37:15.9125330(5)	06:10:13.59548(2)	06:13:43.9756980(10)
Declination, Dec. (J2000)	+41:30:45.2900(3)	−47:15:09.208600(5)	−21:00:27.9314(3)	−02:00:47.22547(3)
Proper motion in RA (mas yr^{-1})	0.0(4)	121.443(1)	9.04(8)	1.828(5)
Proper motion in Dec. (mas yr^{-1})	−4.4(8)	−71.474(2)	16.7(1)	−10.35(1)
Spin frequency, f (s^{-1})	303.090974733986(5)	173.6879457375201(9)	258.9784751479(1)	326.6005620234881(4)
$\dot{f}$ (s^{-2})	$-6.47(1) \times 10^{-16}$	$-1.728350(8) \times 10^{-15}$	$-8.25(1) \times 10^{-16}$	$-1.022962(5) \times 10^{-15}$
Parallax, π (mas)	0.4(4)	6.42(7)	–	0.90(4)
Dispersion measure, DM (cm^{-3} pc)	49.5787(2)	2.6453(3)	60.67(2)	38.7773(5)
$\dot{\mathrm{DM}}$ (cm^{-3} pc yr^{-1})	$8(1) \times 10^{-4}$	$-1(1) \times 10^{-4}$	$-1.0(7) \times 10^{-2}$	$-1(1) \times 10^{-4}$
$\ddot{\mathrm{DM}}$ (cm^{-3} pc yr^{-2})	$3(2) \times 10^{-4}$	$-1(1) \times 10^{-5}$	$1.8(10) \times 10^{-3}$	$1(2) \times 10^{-5}$
Binary model	–	T2	T2	T2
Orbital period, P_b (d)	–	5.7410458(3)	0.28601600622(7)	1.198512575217(10)
Epoch of periastron, T_0 (MJD)	–	55316.6954(3)	55530.88(1)	53862.990(5)
Projected semi-major axis, x (lt-s)	–	3.36672001(5)	0.0734891(3)	1.0914423(3)
Longitude of periastron, ω_0 (deg)	–	1.38(2)	62(15)	37(1)
Eccentricity, e	–	$1.9182(1) \times 10^{-5}$	$2.8(7) \times 10^{-5}$	$4.50(9) \times 10^{-6}$
Sine of inclination, $\sin i$	–	–	–	0.94(2)
Companion mass, m_c ($\mathrm{M}_\odot$)	–	0.228(6)	–	0.14(3)
Derivative of P_b, $\dot{P}_\mathrm{b}$	–	$3.730(3) \times 10^{-12}$	$-2(2) \times 10^{-13}$	$2.6(7) \times 10^{-14}$
Periastron advance $\dot{\omega}_0$ (deg yr^{-1})	–	0.013(1)	–	–
Epoch of ascending node, T_asc (MJD)	–	–	55530.8296112(3)	53862.866713717(8)
$\epsilon_1 = e\sin\omega_0$	–	–	$2.5(7) \times 10^{-5}$	$2.7(1) \times 10^{-6}$
$\epsilon_2 = e\cos\omega_0$	–	–	$1.3(7) \times 10^{-5}$	$3.60(4) \times 10^{-6}$
Longitude of ascending node, Ω (deg)	–	209(1)	–	–
Inclination angle, i (deg)	–	137.51(2)	–	–

Table A1 – *continued*

	J0621+1002	J0645+5158	J0711−6830	J0751+1807
MJD range	52481−56782	55703−56587	49373−55620	50363−56794
Number of ToAs	682	2891	507	1491
Weighted rms timing residual (μs)	9.52	0.92	1.44	3.01
Reduced χ^2	1.01	1.00	1.00	1.01
Reference epoch	55000	56143	55000	55000
Units	TCB	TCB	TCB	TCB
Right ascension, RA (J2000)	06:21:22.11438(2)	06:45:59.081909(4)	07:11:54.18529(1)	07:51:09.15535(2)
Declination, Dec. (J2000)	+10:02:38.734(2)	+51:58:14.92069(8)	−68:30:47.39498(7)	+18:07:38.487(1)
Proper motion in RA (mas yr^{-1})	3.2(1)	1.64(8)	−15.57(2)	−2.72(6)
Proper motion in Dec. (mas yr^{-1})	−0.6(5)	−7.2(1)	14.21(2)	−13.4(3)
Spin frequency, f (s^{-1})	34.657406621409(3)	112.9497214429707(10)	182.117234647221(2)	287.457853995101(4)
$\dot{f}$ (s^{-2})	$-5.683(7) \times 10^{-17}$	$-6.25(2) \times 10^{-17}$	$-4.9438(2) \times 10^{-16}$	$-6.4349(4) \times 10^{-16}$
Parallax, π (mas)	–	0.39(8)	–	0.8(2)
Dispersion measure, DM (cm^{-3} pc)	36.515(6)	18.2479(4)	18.4074(3)	30.247(7)
$\dot{\mathrm{DM}}$ (cm^{-3} pc yr^{-1})	$-7(2) \times 10^{-3}$	$4(3) \times 10^{-5}$	$2(1) \times 10^{-4}$	$0(3) \times 10^{-4}$
$\ddot{\mathrm{DM}}$ (cm^{-3} pc yr^{-2})	$1.1(6) \times 10^{-3}$	$1.3(4) \times 10^{-4}$	$5(3) \times 10^{-5}$	$3(4) \times 10^{-5}$
Binary model	T2	–	–	T2
Orbital period, P_b (d)	8.3186812(3)	–	–	0.263144270733(4)
Epoch of periastron, T_0 (MJD)	55145.69085(4)	–	–	53578.341(8)
Projected semi-major axis, x (lt-s)	12.0320732(4)	–	–	0.3966144(2)
Longitude of periastron, ω_0 (deg)	188.941(2)	–	–	81(11)
Eccentricity, e	0.00245725(7)	–	–	$3.2(6) \times 10^{-6}$
Derivative of P_b, $\dot{P}_b$	–	–	–	$-3.5(3) \times 10^{-14}$
Derivative of x, $\dot{x}$	–	–	–	$-5(1) \times 10^{-15}$
Periastron advance $\dot{\omega}_0$ (deg yr^{-1})	0.0114(6)	–	–	–
Third harmonic of Shapiro, h_3 (s)	–	–	–	$2.7(6) \times 10^{-7}$
Ratio of harmonics amplitude, ζ	–	–	–	0.97(5)
Epoch of ascending node, T_{asc} (MJD)	–	–	–	53578.28170582(2)
$\epsilon_1 = e\sin\omega_0$	–	–	–	$3.1(6) \times 10^{-6}$
$\epsilon_2 = e\cos\omega_0$	–	–	–	$5(6) \times 10^{-7}$

	J0900−3144	J0931−1902	J1012+5307	J1022+1001
MJD range	54286−56795	56350−56587	50646−56796	50360−56769
Number of ToAs	875	712	13056	1399
Weighted rms timing residual (μs)	3.21	3.69	2.05	2.07
Reduced χ^2	1.02	1.00	1.00	0.97
Reference epoch	55000	56469	55000	55000
Units	TCB	TCB	TCB	TCB
Right ascension, RA (J2000)	09:00:43.953111(8)	09:31:19.1174(2)	10:12:33.437530(6)	–
Declination, Dec. (J2000)	−31:44:30.8951(1)	−19:02:55.022(2)	+53:07:02.30019(6)	–
Ecliptic longitude λ (deg)	–	–	–	153.86586693(2)[a]
Ecliptic latitude β (deg)	–	–	–	−0.06389(2)[a]
Proper motion in RA (mas yr^{-1})	−1.00(5)	–	2.61(1)	–
Proper motion in Dec. (mas yr^{-1})	2.01(6)	–	−25.49(1)	–
Proper motion in λ (mas yr^{-1})	–	–	–	−15.93(2)[a]
Proper motion in β (mas yr^{-1})	–	–	–	6(15)[a]
Spin frequency, f (s^{-1})	90.011841919360(4)	215.6088071342(1)	190.2678344415543(8)	60.7794479566968(4)
$\dot{f}$ (s^{-2})	$-3.9604(8) \times 10^{-16}$	$-1.9(3) \times 10^{-16}$	$-6.20045(7) \times 10^{-16}$	$-1.60094(5) \times 10^{-16}$
Parallax, π (mas)	0.7(6)	−2(3)	0.9(2)	0.8(2)
Dispersion measure, DM (cm^{-3} pc)	75.706(7)	41.4880(2)	9.0218(1)	10.253(4)
$\dot{\mathrm{DM}}$ (cm^{-3} pc yr^{-1})	$1.2(7) \times 10^{-3}$	$-2(5) \times 10^{-4}$	$1.0(3) \times 10^{-4}$	$1(9) \times 10^{-5}$
$\ddot{\mathrm{DM}}$ (cm^{-3} pc yr^{-2})	$-2(3) \times 10^{-4}$	–	$1.1(5) \times 10^{-5}$	$3(2) \times 10^{-5}$
Binary model	T2	–	T2	DDH
Orbital period, P_b (d)	18.7376360594(9)	–	0.6046727230 85(3)	7.805136(1)
Epoch of periastron, T_0 (MJD)	55530.415(5)	–	53720.56(1)	53899.5196(2)
Projected semimajor axis, x (lt-s)	17.2488113(2)	–	0.58181754(6)	16.765411(2)
Longitude of periastron, ω_0 (deg)	70.4(1)	–	83(7)	97.775(8)
Eccentricity, e	$1.049(2) \times 10^{-5}$	–	$1.1(1) \times 10^{-6}$	$9.704(5) \times 10^{-5}$
Derivative of P_b, $\dot{P}_b$	–	–	$5.2(4) \times 10^{-14}$	$2.1(7) \times 10^{-13}$
Derivative of x, $\dot{x}$	–	–	$1.9(3) \times 10^{-15}$	$1.31(10) \times 10^{-14}$
Periastron advance $\dot{\omega}_0$ (deg yr^{-1})	–	–	–	0.013(2)
Third harmonic of Shapiro, h_3 (s)	–	–	–	$6.2(7) \times 10^{-7}$

Table A1 – *continued*

Ratio of harmonics amplitude, ζ	–	–	–	0.67(9)
Epoch of ascending node, $T_{\rm asc}$ (MJD)	55526.75096922(3)	–	53720.42199741(1)	–
$\epsilon_1 = e\sin\omega_0$	$9.88(2) \times 10^{-6}$	–	$1.1(1) \times 10^{-6}$	–
$\epsilon_2 = e\cos\omega_0$	$3.52(2) \times 10^{-6}$	–	$1(1) \times 10^{-7}$	–
	J1024-0719	J1045-4509	J1455-3330	J1600-3053
MJD range	50117−56766	49406−55620	53217−56752	52301−56796
Number of ToAs	5865	605	5507	9006
Weighted rms timing residual (μs)	7.29	3.19	4.13	0.95
Reduced χ^2	0.98	1.00	1.01	1.00
Reference epoch	55000	55000	55000	55000
Units	TCB	TCB	TCB	TCB
Right ascension, RA (J2000)	10:24:38.675401(3)	10:45:50.18621(2)	14:55:47.969867(9)	16:00:51.903355(3)
Declination, Dec. (J2000)	−07:19:19.43375(10)	−45:09:54.1151(2)	−33:30:46.3804(2)	−30:53:49.3751(1)
Proper motion in RA (mas yr^{-1})	−35.27(2)	−6.08(6)	7.91(4)	−0.97(1)
Proper motion in Dec. (mas yr^{-1})	−48.22(4)	5.15(6)	−1.90(9)	−7.04(5)
Spin frequency, f (s^{-1})	193.7156834485 25(4)	133.793149541188(3)	125.2002432449954(4)	277.9377069896082(8)
$\dot{f}$ (s^{-2})	$-6.9544(3) \times 10^{-16}$	$-3.1621(3) \times 10^{-16}$	$-3.80953(8) \times 10^{-16}$	$-7.3385(2) \times 10^{-16}$
Parallax, π (mas)	0.8(1)	–	0.9(2)	0.50(6)
Dispersion measure, DM (cm^{-3} pc)	6.4765(8)	58.144(6)	13.5692(2)	52.3310(3)
$\dot{\rm DM}$ (cm^{-3} pc yr^{-1})	$2.8(8) \times 10^{-4}$	$0(3) \times 10^{-3}$	$1.8(2) \times 10^{-4}$	$-3.6(5) \times 10^{-4}$
$\ddot{\rm DM}$ (cm^{-3} pc yr^{-2})	$0(2) \times 10^{-5}$	$1(2) \times 10^{-4}$	$1(6) \times 10^{-6}$	$6(2) \times 10^{-5}$
Binary model	–	T2	T2	DDH
Orbital period, $P_{\rm b}$ (d)	–	4.0835292548(2)	76.174568646(4)	14.348463(1)
Epoch of periastron, T_0 (MJD)	–	54523.124(4)	54921.7489(5)	55232.5810(3)
Projected semi-major axis, x (lt-s)	–	3.0151315(2)	32.3622132(2)	8.8016537(4)
Longitude of periastron, ω_0 (deg)	–	242.1(3)	223.457(2)	181.838(7)
Eccentricity, e	–	$2.34(1) \times 10^{-5}$	$1.69663(7) \times 10^{-4}$	$1.73726(5) \times 10^{-4}$
Derivative of x, $\dot{x}$	–	–	$-2.1(2) \times 10^{-14}$	$-3.3(3) \times 10^{-15}$
Periastron advance $\dot{\omega}_0$ (deg yr^{-1})	–	–	–	0.0031(7)
Third harmonic of Shapiro, h_3 (s)	–	–	–	$3.5(2) \times 10^{-7}$
Ratio of harmonics amplitude, ζ	–	–	–	0.67(3)
	J1603−7202	J1614−2230	J1640+2224	J1643−1224
MJD range	50025−55620	54724−56587	50458−56762	49422−56778
Number of ToAs	463	7323	3098	8136
Weighted rms timing residual (μs)	1.66	1.38	0.85	3.23
Reduced χ^2	0.93	1.00	0.97	1.00
Reference epoch	55000	55655	55000	55000
Units	TCB	TCB	TCB	TCB
Right ascension, RA (J2000)	16:03:35.67676(3)	16:14:36.50712(2)	16:40:16.744853(3)	16:43:38.161543(10)
Declination, Dec. (J2000)	−72:02:32.7400(2)	−22:30:31.231(2)	+22:24:08.84115(7)	−12:24:58.6731(7)
Proper motion in RA (mas yr^{-1})	−2.47(3)	3.6(2)	2.08(1)	6.03(3)
Proper motion in Dec. (mas yr^{-1})	−7.36(4)	−33(1)	−11.34(2)	4.1(1)
Spin frequency, f (s^{-1})	67.376581128781(1)	317.3789370687213(7)	316.12397933185 61(6)	216.373337142635(7)
$\dot{f}$ (s^{-2})	$-7.094(1) \times 10^{-17}$	$-9.6945(3) \times 10^{-16}$	$-2.81540(7) \times 10^{-16}$	$-8.6440(4) \times 10^{-16}$
Parallax, π (mas)	–	1.46(9)	0.6(4)	0.9(3)
Dispersion measure, DM (cm^{-3} pc)	38.059(5)	34.4907(2)	18.4268(2)	62.414(1)
$\dot{\rm DM}$ (cm^{-3} pc yr^{-1})	$3(6) \times 10^{-4}$	$-7(5) \times 10^{-5}$	$9(3) \times 10^{-5}$	$-1.1(7) \times 10^{-3}$
$\ddot{\rm DM}$ (cm^{-3} pc yr^{-2})	$4(7) \times 10^{-5}$	$4(7) \times 10^{-5}$	$-1.8(6) \times 10^{-5}$	$-6(7) \times 10^{-5}$
Binary model	T2	ELL1	T2	T2
Orbital period, $P_{\rm b}$ (d)	6.3086296703(2)	8.68661955647(8)	175.46064(2)	147.01739778(1)
Epoch of periastron, T_0 (MJD)	54523.571(5)	55662.388(9)	54258.0894(2)	53547.4385(3)
Projected semi-major axis, x (lt-s)	6.8806626(1)	11.29119760(7)	55.3297216(5)	25.0725970(2)
Longitude of periastron, ω_0 (deg)	170.2(3)	175.8(4)	50.7323(4)	321.8494(7)
Eccentricity, e	$9.35(4) \times 10^{-6}$	$1.334(7) \times 10^{-6}$	$7.97272(6) \times 10^{-4}$	$5.05749(6) \times 10^{-4}$
Sine of inclination, $\sin i$	–	0.999899(3)	0.973(9)	–
Companion mass, $m_{\rm c}$ ($M_\odot$)	–	0.494(2)	0.18(4)	–
Derivative of $P_{\rm b}$, $\dot{P}_{\rm b}$	$3(1) \times 10^{-13}$	–	–	–
Derivative of x, $\dot{x}$	$1.5(1) \times 10^{-14}$	–	$1.2(1) \times 10^{-14}$	$-5.1(1) \times 10^{-14}$
Periastron advance $\dot{\omega}_0$ (deg yr^{-1})	–	–	$-9(7) \times 10^{-5}$	–
Epoch of ascending node, $T_{\rm asc}$ (MJD)	–	55658.145541895(5)	–	–
$\epsilon_1 = e\sin\omega_0$	–	$9.7(9) \times 10^{-8}$	–	–
$\epsilon_2 = e\cos\omega_0$	–	$-1.331(7) \times 10^{-6}$	–	–

Table A1 *– continued*

	J1713+0747	J1721−2457	J1730−2304	J1732−5049
MJD range	48849−57053	52076−56737	49422−56831	52646−55583
Number of ToAs	17487	150	646	242
Weighted rms timing residual (μs)	0.24	12.21	1.67	2.80
Reduced χ^2	0.99	0.98	0.92	0.92
Reference epoch	55000	55000	55000	55000
Units	TCB	TCB	TCB	TCB
Right ascension, RA (J2000)	17:13:49.5331960(4)	17:21:05.4980(2)	17:30:21.66836(7)	17:32:47.76668(2)
Declination, Dec. (J2000)	+07:47:37.49256(1)	−24:57:06.17(4)	−23:04:31.17(2)	−50:49:00.2052(4)
Proper motion in RA (mas yr^{-1})	4.924(1)	2(1)	20.2(3)	−0.37(8)
Proper motion in Dec. (mas yr^{-1})	−3.913(2)	−26(14)	−1(6)	−9.9(2)
Spin frequency, f (s^{-1})	218.8118404171579(7)	285.9893434446(4)	123.1102871473768(9)	188.233512191560(6)
$\dot{f}$ (s^{-2})	$-4.08386(5) \times 10^{-16}$	$-4.54(5) \times 10^{-16}$	$-3.0587(1) \times 10^{-16}$	$-5.029(1) \times 10^{-16}$
Parallax, π (mas)	0.83(2)	–	1.7(2)	–
Dispersion measure, DM (cm^{-3} pc)	15.969(3)	48.3(1)	9.615(3)	56.8399(7)
$\dot{\mathrm{DM}}$ (cm^{-3} pc yr^{-1})	$-2(3) \times 10^{-5}$	−0.01(2)	0.0011(2)	$9(6) \times 10^{-4}$
$\ddot{\mathrm{DM}}$ (cm^{-3} pc yr^{-2})	$-3(3) \times 10^{-6}$	−0.001(4)	$1.0(3) \times 10^{-4}$	$1(2) \times 10^{-4}$
Binary model	T2	–	–	ELL1
Orbital period, P_b (d)	67.825131000(1)	–	–	5.2629972000(4)
Epoch of periastron, T_0 (MJD)	52811.4820(2)	–	–	51398.79(1)
Projected semi-major axis, x (lt-s)	32.34242200(8)	–	–	3.9828703(3)
Longitude of periastron, ω_0 (deg)	176.1987(9)	–	–	166(1)
Eccentricity, e	$7.49402(4) \times 10^{-5}$	–	–	$8.4(1) \times 10^{-6}$
Companion mass, m_c ($\mathrm{M}_\odot$)	0.289(7)	–	–	–
Derivative of P_b, $\dot{P}_\mathrm{b}$	$5(1) \times 10^{-13}$	–	–	–
Epoch of ascending node, T_asc (MJD)	–	–	–	51396.3661226(2)
$\epsilon_1 = e\sin\omega_0$	–	–	–	$2.0(2) \times 10^{-6}$
$\epsilon_2 = e\cos\omega_0$	–	–	–	$-8.2(1) \times 10^{-6}$
Longitude of ascending node, Ω (deg)	92(2)	–	–	–
Inclination angle, i (deg)	71.6(4)	–	–	–

	J1738+0333	J1741+1351	J1744−1134	J1747−4036
MJD range	54102−56781	55041−56595	49728−56992	55976−56587
Number of ToAs	2941	1588	9834	2771
Weighted rms timing residual (μs)	1.42	0.47	0.81	4.79
Reduced χ^2	0.98	0.99	0.99	0.99
Reference epoch	55000	55818	55000	56281
Units	TCB	TCB	TCB	TCB
Right ascension, RA (J2000)	17:38:53.966385(9)	17:41:31.145389(3)	17:44:29.4075540(8)	17:47:48.71664(1)
Declination, Dec. (J2000)	+03:33:10.8723(4)	+13:51:44.13006(6)	−11:34:54.69427(6)	−40:36:54.7802(7)
Proper motion in RA (mas yr^{-1})	7.12(4)	−8.96(3)	18.797(4)	−0.2(8)
Proper motion in Dec. (mas yr^{-1})	5.0(1)	−7.57(4)	−9.41(2)	−5(1)
Spin frequency, f (s^{-1})	170.937369887091(8)	266.869162906907(1)	245.4261196898085(5)	607.67752932437(1)
$\dot{f}$ (s^{-2})	$-7.0459(9) \times 10^{-16}$	$-2.15196(4) \times 10^{-15}$	$-5.38164(4) \times 10^{-16}$	$-4.856(4) \times 10^{-15}$
Parallax, π (mas)	–	0.5(2)	2.44(5)	0.4(7)
Dispersion measure, DM (cm^{-3} pc)	33.777(1)	24.19954(4)	3.1395(2)	152.9652(7)
$\dot{\mathrm{DM}}$ (cm^{-3} pc yr^{-1})	$-1.7(7) \times 10^{-3}$	$-2.9(6) \times 10^{-4}$	$-5(1) \times 10^{-5}$	$-5.8(4) \times 10^{-3}$
$\ddot{\mathrm{DM}}$ (cm^{-3} pc yr^{-2})	$2(1) \times 10^{-4}$	$4(3) \times 10^{-5}$	$1.0(3) \times 10^{-5}$	$0(3) \times 10^{-3}$
Binary model	T2	ELL1	–	–
Orbital period, P_b (d)	0.35479073985(1)	16.3353480804(7)	–	–
Epoch of periastron, T_0 (MJD)	55441.84(1)	55828.511(5)	–	–
Projected semimajor axis, x (lt-s)	0.34343014(9)	11.0033167(2)	–	–
Longitude of periastron, ω_0 (deg)	74(14)	204.0(1)	–	–
Eccentricity, e	$1.8(4) \times 10^{-6}$	$1.000(1) \times 10^{-5}$	–	–
Companion mass, m_c ($\mathrm{M}_\odot$)	–	0.15(1)	–	–
Derivative of x, $\dot{x}$	–	$-7(2) \times 10^{-15}$	–	–
Epoch of ascending node, T_asc (MJD)	55441.76403507(4)	55819.25488144(3)	–	–
$\epsilon_1 = e\sin\omega_0$	$1.8(4) \times 10^{-6}$	$-4.06(2) \times 10^{-6}$	–	–
$\epsilon_2 = e\cos\omega_0$	$5(5) \times 10^{-7}$	$-9.13(1) \times 10^{-6}$	–	–

Table A1 – *continued*

	J1751−2857	J1801−1417	J1802−2124	J1804−2717
MJD range	53746−56782	54206−56782	54187−56832	53766−56828
Number of ToAs	144	126	522	116
Weighted rms timing residual (μs)	3.12	2.76	2.76	3.72
Reduced χ^2	0.92	0.90	1.02	0.98
Reference epoch	55000	55000	55000	55000
Units	TCB	TCB	TCB	TCB
Right ascension, RA (J2000)	17:51:32.69320(2)	18:01:51.07335(2)	18:02:05.33524(2)	18:04:21.13311(2)
Declination, Dec. (J2000)	−28:57:46.521(3)	−14:17:34.527(2)	−21:24:03.654(8)	−27:17:31.335(4)
Proper motion in RA (mas yr^{-1})	−7.4(1)	−10.9(1)	−1.1(1)	2.6(2)
Proper motion in Dec. (mas yr^{-1})	−4(1)	−3.1(9)	−4(4)	−18(2)
Spin frequency, f (s^{-1})	255.4361108856(2)	275.8547089970(1)	79.066422943038(9)	107.03164921949(4)
$\dot{f}$ (s^{-2})	$-7.31(2) \times 10^{-16}$	$-4.03(2) \times 10^{-16}$	$-4.558(2) \times 10^{-16}$	$-4.680(5) \times 10^{-16}$
Parallax, π (mas)	–	–	1.2(7)	–
Dispersion measure, DM (cm^{-3} pc)	42.85(3)	57.25(3)	149.614(9)	24.73(3)
$\dot{\mathrm{DM}}$ (cm^{-3} pc yr^{-1})	−0.01(1)	0.004(6)	$-1(2) \times 10^{-3}$	−0.006(6)
$\ddot{\mathrm{DM}}$ (cm^{-3} pc yr^{-2})	0.001(2)	0.001(2)	$6(6) \times 10^{-4}$	0.000(1)
Binary model	T2	–	T2	T2
Orbital period, P_b (d)	110.74646081(4)	–	0.698889254217(8)	11.128711966(3)
Epoch of periastron, T_0 (MJD)	55260.235(3)	–	55509.53(1)	55290.721(9)
Projected semi-major axis, x (lt-s)	32.5282325(4)	–	3.718855(2)	7.2814525(7)
Longitude of periastron, ω_0 (deg)	45.51(1)	–	31(6)	158.6(3)
Eccentricity, e	$1.2795(3) \times 10^{-4}$	–	$3.1(2) \times 10^{-6}$	$3.41(2) \times 10^{-5}$
Sine of inclination, $\sin i$	–	–	0.979(9)	–
Companion mass, m_c ($\mathrm{M}_\odot$)	–	–	0.7(2)	–
Derivative of x, $\dot{x}$	$4.5(7) \times 10^{-14}$	–	–	–
Epoch of ascending node, T_asc (MJD)	–	–	55509.46452585(1)	–
$\epsilon_1 = e\sin\omega_0$	–	–	$1.6(4) \times 10^{-6}$	–
$\epsilon_2 = e\cos\omega_0$	–	–	$2.6(2) \times 10^{-6}$	–

	J1824−2452A	J1832−0836	J1843−1113	J1853+1303
MJD range	53518−55583	56353−56587	53156−56829	53762−56831
Number of ToAs	276	1131	224	1470
Weighted rms timing residual (μs)	1.83	1.94	0.97	1.31
Reduced χ^2	0.95	1.00	0.95	1.00
Reference epoch	55000	56475	55000	55000
Units	TCB	TCB	TCB	TCB
Right ascension, RA (J2000)	18:24:32.00790(3)	18:32:27.5936(2)	18:43:41.26193(1)	18:53:57.318794(4)
Declination, Dec. (J2000)	−24:52:10.848(8)	−08:36:55.00(4)	−11:13:31.0688(7)	+13:03:44.06902(9)
Proper motion in RA (mas yr^{-1})	−0.2(2)	–	−1.91(6)	−1.63(2)
Proper motion in Dec. (mas yr^{-1})	−6(4)	–	−3.2(2)	−2.96(4)
Spin frequency, f (s^{-1})	327.40558298353(1)	367.7671154916(2)	541.8097450362(2)	244.391374031064(6)
$\dot{f}$ (s^{-2})	$-1.735305(2) \times 10^{-13}$	$-1.1(2) \times 10^{-15}$	$-2.803(2) \times 10^{-15}$	$-5.2065(7) \times 10^{-16}$
Parallax, π (mas)	–	1(5)	0.6(4)	0.2(3)
Dispersion measure, DM (cm^{-3} pc)	119.8907(7)	28.1910(1)	59.964(8)	30.5694(6)
$\dot{\mathrm{DM}}$ (cm^{-3} pc yr^{-1})	0.001(2)	0.0013(2)	0.001(4)	$6(4) \times 10^{-4}$
$\ddot{\mathrm{DM}}$ (cm^{-3} pc yr^{-2})	−0.0002(5)	0.010(1)	0.0011(10)	$-1.4(7) \times 10^{-4}$
Binary model	–	–	–	T2
Orbital period, P_b (d)	–	–	–	115.653788229(7)
Epoch of periastron, T_0 (MJD)	–	–	–	55203.339(4)
Projected semi-major axis, x (lt-s)	–	–	–	40.7695221(1)
Longitude of periastron, ω_0 (deg)	–	–	–	346.67(1)
Eccentricity, e	–	–	–	$2.3697(5) \times 10^{-5}$
Derivative of x, $\dot{x}$	–	–	–	$1.4(2) \times 10^{-14}$

	J1857+0943	J1903+0327	J1909−3744	J1910+1256
MJD range	46401−56782	55135−56593	53040−56993	53370−56829
Number of ToAs	5004	1802	11483	2743
Weighted rms timing residual (μs)	1.25	2.85	0.20	1.42
Reduced χ^2	0.99	0.98	1.00	1.01
Reference epoch	55000	55712	55000	55000
Units	TCB	TCB	TCB	TCB
Right ascension, RA (J2000)	18:57:36.390622(3)	19:03:05.79288(2)	19:09:47.4335840(4)	19:10:09.701469(6)
Declination, Dec. (J2000)	+09:43:17.20712(7)	+03:27:19.195(1)	−37:44:14.51573(2)	+12:56:25.4867(1)
Proper motion in RA (mas yr^{-1})	−2.652(4)	−2.8(3)	−9.513(2)	0.21(3)

Table A1 *– continued*

Proper motion in Dec. (mas yr^{-1})	−5.423(6)	−6.6(8)	−35.777(6)	−7.04(5)
Spin frequency, f (s^{-1})	186.4940783779782(8)	465.13523808900(2)	339.3156872184837(1)	200.658802230121(2)
$\dot{f}$ (s^{-2})	$-6.20446(6) \times 10^{-16}$	$-4.070(1) \times 10^{-15}$	$-1.614819(4) \times 10^{-15}$	$-3.8975(2) \times 10^{-16}$
Parallax, π (mas)	0.9(1)	0.3(7)	0.88(1)	0.1(3)
Dispersion measure, DM (cm^{-3} pc)	13.311(3)	297.552(6)	10.39217(4)	38.065(1)
$\dot{\mathrm{DM}}$ (cm^{-3} pc yr^{-1})	$2(1) \times 10^{-4}$	0.000(2)	−0.00027(1)	$7(2) \times 10^{-4}$
$\ddot{\mathrm{DM}}$ (cm^{-3} pc yr^{-2})	$3.2(9) \times 10^{-5}$	−0.003(2)	0.000012(5)	$0(1) \times 10^{-4}$
Binary model	T2	T2	T2	T2
Orbital period, P_b (d)	12.32717138213(4)	95.17411881(4)	1.533449475278(1)	58.466742968(3)
Epoch of periastron, T_0 (MJD)	53619.522(1)	55776.9745388(2)	55016.13(2)	55073.2517(4)
Projected semi-major axis, x (lt-s)	9.2307805(1)	105.593464(2)	1.89799110(2)	21.1291023(1)
Longitude of periastron, ω_0 (deg)	276.47(3)	141.6536044(9)	165(6)	106.009(2)
Eccentricity, e	$2.167(2) \times 10^{-5}$	0.43667841(1)	$1.04(6) \times 10^{-7}$	$2.30233(10) \times 10^{-4}$
Sine of inclination, $\sin i$	0.9993(1)	0.97(1)	0.99807(6)	–
Companion mass, m_c ($\mathrm{M}_\odot$)	0.245(7)	1.1(1)	0.209(1)	–
Derivative of P_b, $\dot{P}_\mathrm{b}$	–	–	$5.05(3) \times 10^{-13}$	–
Derivative of x, $\dot{x}$	$-4(2) \times 10^{-16}$	–	$-3.9(7) \times 10^{-16}$	$-1.7(1) \times 10^{-14}$
Periastron advance $\dot{\omega}_0$ (deg yr^{-1})	–	$2.404(7) \times 10^{-4}$	–	–
Epoch of ascending node, T_asc (MJD)	–	–	55015.4280907538(10)	–
$\epsilon_1 = e\sin\omega_0$	–	–	$3(1) \times 10^{-8}$	–
$\epsilon_2 = e\cos\omega_0$	–	–	$-1.01(6) \times 10^{-7}$	–
	J1911−1114	J1911+1347	J1918−0642	J1923+2515
MJD range	53815−57028	54096−56827	52094−56770	55790−56595
Number of ToAs	130	140	9942	920
Weighted rms timing residual (μs)	4.82	1.09	1.81	2.25
Reduced χ^2	0.97	0.95	1.00	0.99
Reference epoch	55000	55000	55000	56100
Units	TCB	TCB	TCB	TCB
Right ascension, RA (J2000)	19:11:49.28235(3)	19:11:55.204700(5)	19:18:48.033136(3)	19:23:22.493361(8)
Declination, Dec. (J2000)	−11:14:22.482(2)	+13:47:34.3839(1)	−06:42:34.8895(1)	+25:15:40.6165(2)
Proper motion in RA (mas yr^{-1})	−13.7(2)	−2.90(3)	−7.15(2)	−6.69(10)
Proper motion in Dec. (mas yr^{-1})	−9.3(9)	−3.76(5)	−5.94(5)	−14.7(2)
Spin frequency, f (s^{-1})	275.8053380432(3)	216.17122737198(2)	130.7895141233725(2)	263.980710176120(6)
$\dot{f}$ (s^{-2})	$-1.060(3) \times 10^{-15}$	$-7.908(3) \times 10^{-16}$	$-4.39472(5) \times 10^{-16}$	$-6.663(4) \times 10^{-16}$
Parallax, π (mas)	–	–	0.8(1)	−0.3(6)
Dispersion measure, DM (cm^{-3} pc)	31.0(1)	30.987(6)	26.578(5)	18.8553(3)
$\dot{\mathrm{DM}}$ (cm^{-3} pc yr^{-1})	−0.03(2)	$0(2) \times 10^{-3}$	$-1.9(6) \times 10^{-4}$	$-3(4) \times 10^{-5}$
$\ddot{\mathrm{DM}}$ (cm^{-3} pc yr^{-2})	0.004(3)	$1(4) \times 10^{-4}$	$1(2) \times 10^{-5}$	$-1(4) \times 10^{-5}$
Binary model	T2	–	DDH	–
Orbital period, P_b (d)	2.7165576620(7)	–	10.9131777492(1)	–
Epoch of periastron, T_0 (MJD)	55422.4(3)	–	54424.111(1)	–
Projected semi-major axis, x (lt-s)	1.7628746(9)	–	8.3504663(2)	–
Longitude of periastron, ω_0 (deg)	125(38)	–	219.51(4)	–
Eccentricity, e	$1.4(10) \times 10^{-6}$	–	$2.035(1) \times 10^{-5}$	–
Third harmonic of Shapiro, h_3 (s)	–	–	$8.8(2) \times 10^{-7}$	–
Ratio of harmonics amplitude, ζ	–	–	0.910(7)	–
Epoch of ascending node, T_asc (MJD)	55421.4791904(2)	–	–	–
$\epsilon_1 = e\sin\omega_0$	$1(1) \times 10^{-6}$	–	–	–
$\epsilon_2 = e\cos\omega_0$	$-8(9) \times 10^{-7}$	–	–	–
	J1939+2134	J1944+0907	J1949+3106	J1955+2908
MJD range	46024−56779	54505−56593	56138−56595	53812−56782
Number of ToAs	13659	1696	1409	1459
Weighted rms timing residual (μs)	50.63	2.23	4.61	3.62
Reduced χ^2	0.94	0.99	1.00	1.00
Reference epoch	55000	55000	56367	55000
Units	TCB	TCB	TCB	TCB
Right ascension, RA (J2000)	19:39:38.561249(2)	19:44:09.32685(2)	19:49:29.6373(2)	19:55:27.87578(1)
Declination, Dec. (J2000)	+21:34:59.12551(3)	+09:07:23.1091(6)	+31:06:03.802(2)	+29:08:43.4593(2)
Proper motion in RA (mas yr^{-1})	0.074(2)	14.14(8)	−5(5)	−1.03(6)
Proper motion in Dec. (mas yr^{-1})	−0.410(3)	−22.6(2)	−5(7)	−4.17(8)
Spin frequency, f (s^{-1})	641.92822458217(2)	192.856517920199(3)	76.11402373420(1)	163.04791050691(2)

Table A1 – *continued*

$\dot{f}$ (s^{-2})	−4.331255(7)	$-6.4488(3) \times 10^{-16}$	$-5.44(8) \times 10^{-16}$	$-7.908(2) \times 10^{-16}$
Parallax, π (mas)	0.19(5)	0.1(3)	−1(3)	−1(1)
Dispersion measure, DM (cm^{-3} pc)	71.11(2)	24.3514(7)	164.1263(7)	104.516(3)
$\dot{DM}$ (cm^{-3} pc yr^{-1})	$-2(3) \times 10^{-4}$	$1.7(8) \times 10^{-3}$	$5(8) \times 10^{-4}$	$3(2) \times 10^{-3}$
$\ddot{DM}$ (cm^{-3} pc yr^{-2})	$2(2) \times 10^{-5}$	$0(3) \times 10^{-4}$	$-3(4) \times 10^{-3}$	$-6(4) \times {}^{-4}$
Binary model	–	–	ELL1	T2
Orbital period, P_b (d)	–	–	1.9495344460(4)	117.34909911(2)
Epoch of periastron, T_0 (MJD)	–	–	56367.098(1)	55265.7080(7)
Projected semimajor axis, x (lt-s)	–	–	7.288653(2)	31.4126920(3)
Longitude of periastron, ω_0 (deg)	–	–	207.5(2)	29.479(2)
Eccentricity, e	–	–	$4.30(1) \times 10^{-5}$	$3.3022(2) \times 10^{-4}$
Sine of inclination, $\sin i$	–	–	0.990(5)	–
Companion mass, m_c ($M_\odot$)	–	–	0.6(1)	–
Derivative of x, $\dot{x}$	–	–	–	$1.4(3) \times 10^{-14}$
Epoch of ascending node, T_{asc} (MJD)	–	–	56365.97400000(2)	–
$\epsilon_1 = e\sin\omega_0$	–	–	$-1.99(2) \times 10^{-5}$	–
$\epsilon_2 = e\cos\omega_0$	–	–	$-3.815(9) \times 10^{-5}$	–
	J2010−1323	J2017+0603	J2019+2425	J2033+1734
MJD range	54089−56786	55989−56600	53451−56788	53898−56789
Number of ToAs	8057	1565	130	194
Weighted rms timing residual (μs)	2.55	0.73	9.64	13.65
Reduced χ^2	1.00	0.99	0.97	0.94
Reference epoch	55000	56200	55000	55000
Units	TCB	TCB	TCB	TCB
Right ascension, RA (J2000)	20:10:45.92065(1)	20:17:22.70505(1)	20:19:31.94085(7)	20:33:27.51419(6)
Declination, Dec. (J2000)	−13:23:56.0664(6)	+06:03:05.5688(3)	+24:25:15.013(2)	+17:34:58.525(2)
Proper motion in RA (mas yr^{-1})	2.56(6)	2.4(4)	−8.8(5)	−5.9(4)
Proper motion in Dec. (mas yr^{-1})	−5.9(2)	−0.5(6)	−19.9(7)	−9.0(8)
Spin frequency, f (s^{-1})	191.450909092640(4)	345.27813115158(1)	254.1603414551(5)	168.0966754307(2)
$\dot{f}$ (s^{-2})	$-1.7686(5) \times 10^{-16}$	$-9.53(1) \times 10^{-16}$	$-4.49(4) \times 10^{-16}$	$-3.13(2) \times 10^{-16}$
Parallax, π (mas)	0.2(1)	0.5(2)	–	–
Dispersion measure, DM (cm^{-3} pc)	22.1599(3)	23.9232(1)	17.2(1)	25.0(1)
$\dot{DM}$ (cm^{-3} pc yr^{-1})	$6(3) \times 10^{-4}$	$-5(5) \times 10^{-4}$	−0.04(3)	−0.03(2)
$\ddot{DM}$ (cm^{-3} pc yr^{-2})	$-5(5) \times 10^{-5}$	$8(7) \times 10^{-4}$	0.004(4)	0.002(3)
Binary model	–	ELL1	T2	T2
Orbital period, P_b (d)	–	2.1984811706(2)	76.51163605(8)	56.30779617(6)
Epoch of periastron, T_0 (MJD)	–	56294.07(1)	55104.42(1)	55339.98(1)
Projected semi-major axis, x (lt-s)	–	2.1929203(9)	38.767653(2)	20.163116(2)
Longitude of periastron, ω_0 (deg)	–	178(2)	159.06(5)	78.10(7)
Eccentricity, e	–	$7.00(6) \times 10^{-6}$	$1.1114(10) \times 10^{-4}$	$1.286(1) \times 10^{-4}$
Sine of inclination, $\sin i$	–	0.92(4)	–	–
Companion mass, m_c ($M_\odot$)	–	0.22(10)	–	–
Epoch of ascending node, T_{asc} (MJD)	–	56292.97900647(1)	–	–
$\epsilon_1 = e\sin\omega_0$	–	$2(2) \times 10^{-7}$	–	–
$\epsilon_2 = e\cos\omega_0$	–	$-7.00(6) \times 10^{-6}$	–	–
	J2043+1711	J2124−3358	J2129−5721	J2145−0750
MJD range	55757−56593	49489−56796	49987−55618	49001−56762
Number of ToAs	1382	1182	373	8456
Weighted rms timing residual (μs)	0.63	3.00	1.03	6.08
Reduced χ^2	0.99	0.97	1.04	1.00
Reference epoch	56175	55000	55000	55000
Units	TCB	TCB	TCB	TCB
Right ascension, RA (J2000)	20:43:20.882167(2)	21:24:43.84783(1)	21:29:22.768535(8)	21:45:50.460606(7)
Declination, Dec. (J2000)	+17:11:28.92444(5)	−33:58:44.9190(3)	−57:21:14.22517(9)	−07:50:18.4877(3)
Proper motion in RA (mas yr^{-1})	−5.76(6)	−14.09(3)	9.25(2)	−9.58(3)
Proper motion in Dec. (mas yr^{-1})	−10.8(1)	−50.23(7)	−9.61(3)	−8.87(7)
Spin frequency, f (s^{-1})	420.189436753417(2)	202.793893746028(2)	268.359227293859(3)	62.295887837384(1)
$\dot{f}$ (s^{-2})	$-9.257(1) \times 10^{-16}$	$-8.4596(2) \times 10^{-16}$	$-1.50176(3) \times 10^{-15}$	$-1.15635(9) \times 10^{-16}$
Parallax, π (mas)	0.9(1)	2.6(3)	–	1.54(10)
Dispersion measure, DM (cm^{-3} pc)	20.71185(6)	4.598(3)	31.850(3)	9.0018(6)
$\dot{DM}$ (cm^{-3} pc yr^{-1})	$-9.2(10) \times 10^{-5}$	$1(1) \times 10^{-4}$	$-4(6) \times 10^{-5}$	$1.4(6) \times 10^{-4}$
$\ddot{DM}$ (cm^{-3} pc yr^{-2})	$0(1) \times 10^{-5}$	$0(3) \times 10^{-5}$	$2(2) \times 10^{-5}$	$1.1(8) \times 10^{-5}$

Table A1 – *continued*

Binary model	ELL1	–	T2	T2
Orbital period, P_b (d)	1.4822908095(1)	–	6.6254930961(3)	6.83890261543(3)
Epoch of periastron, T_0 (MJD)	56175.290(4)	–	54626.952(6)	53562.1912(5)
Projected semi-major axis, x (lt-s)	1.6239583(2)	–	3.5005668(1)	10.16410802(8)
Longitude of periastron, ω_0 (deg)	238.9(9)	–	196.8(3)	200.83(3)
Eccentricity, e	$4.87(10) \times 10^{-6}$	–	$1.217(6) \times 10^{-5}$	$1.9318(10) \times 10^{-5}$
Sine of inclination, $\sin i$	0.992(2)	–	–	–
Companion mass, m_c ($M_\odot$)	0.18(1)	–	–	–
Derivative of P_b, $\dot{P}_b$	–	–	$1.1(3) \times 10^{-12}$	$1.3(3) \times 10^{-13}$
Derivative of x, $\dot{x}$	–	–	–	$7.5(5) \times 10^{-15}$
Epoch of ascending node, T_{asc} (MJD)	56174.306442752(9)	–	–	53558.375983405(9)
$\epsilon_1 = e\sin\omega_0$	$-4.2(1) \times 10^{-6}$	–	–	$-6.871(9) \times 10^{-6}$
$\epsilon_2 = e\cos\omega_0$	$-2.51(6) \times 10^{-6}$	–	–	$-1.8055(10) \times 10^{-5}$

	J2214+3000	J2229+2643	J2302+4442	J2317+1439
MJD range	55843–56600	53790–56796	55971–56587	50458–56795
Number of ToAs	2514	316	3037	3175
Weighted rms timing residual (μs)	1.67	4.28	13.70	0.88
Reduced χ^2	1.00	0.99	1.00	0.99
Reference epoch	56222	55000	56279	55000
Units	TCB	TCB	TCB	TCB
Right ascension, RA (J2000)	22:14:38.850999(5)	22:29:50.88544(2)	23:02:46.9786(3)	23:17:09.236650(6)
Declination, Dec. (J2000)	+30:00:38.19752(6)	+26:43:57.6809(3)	+44:42:22.097(3)	+14:39:31.2558(2)
Proper motion in RA (mas yr^{-1})	20.7(1)	−1.7(1)	−5(4)	−1.33(3)
Proper motion in Dec. (mas yr^{-1})	−1.6(2)	−5.9(1)	−7(5)	3.51(5)
Spin frequency, f (s^{-1})	320.592287444895(5)	335.81620819686(1)	192.59196069134(6)	290.2546036648703(6)
$\dot{f}$ (s^{-2})	$-1.5147(6) \times 10^{-15}$	$-1.716(4) \times 10^{-16}$	$-5.2(1) \times 10^{-16}$	$-2.0471(1) \times 10^{-16}$
Parallax, π (mas)	1.1(2)	–	1(1)	0.1(1)
Dispersion measure, DM (cm^{-3} pc)	22.5521(6)	22.71(2)	13.7280(3)	21.8996(3)
$\dot{DM}$ (cm^{-3} pc yr^{-1})	0.0003(2)	$9(5) \times 10^{-4}$	$-3(2) \times 10^{-4}$	$-5.4(7) \times 10^{-4}$
$\ddot{DM}$ (cm^{-3} pc yr^{-2})	−0.0012(4)	$2(3) \times 10^{-4}$	$-2(3) \times 10^{-4}$	$3(2) \times 10^{-5}$
Binary model	ELL1	T2	T2	T2
Orbital period, P_b (d)	0.4166329521(3)	93.01589388(4)	125.93529877(8)	2.45933150334(2)
Epoch of periastron, T_0 (MJD)	56221.81(9)	55279.710(3)	56302.6617(8)	53627.02(5)
Projected semimajor axis, x (lt-s)	0.059 081 16(10)	18.9125229(4)	51.429966(2)	2.3139484(2)
Longitude of periastron, ω_0 (deg)	227(78)	14.34(1)	−152.103(2)	86(7)
Eccentricity, e	$3(4) \times 10^{-6}$	$2.5523(4) \times 10^{-4}$	$5.0303(1) \times 10^{-4}$	$4.1(6) \times 10^{-7}$
Sine of inclination, $\sin i$	–	–	0.98(1)	–
Companion mass, m_c ($M_\odot$)	–	–	0.4(1)	–
Derivative of x, $\dot{x}$	–	–	–	$1.8(7) \times 10^{-15}$
Epoch of ascending node, T_{asc} (MJD)	56221.5468080(2)	–	–	53626.43654694(2)
$\epsilon_1 = e\sin\omega_0$	$-2(5) \times 10^{-6}$	–	–	$4.1(6) \times 10^{-7}$
$\epsilon_2 = e\cos\omega_0$	$-2(3) \times 10^{-6}$	–	–	$3(5) \times 10^{-8}$

	J2322+2057
MJD range	53905–56789
Number of ToAs	229
Weighted rms timing residual (μs)	6.74
Reduced χ^2	0.97
Reference epoch	55000
Units	TCB
Right ascension, RA (J2000)	23:22:22.33519(7)
Declination, Dec. J2000)	+20:57:02.677(1)
Proper motion in RA (mas yr^{-1})	−18.5(3)
Proper motion in Dec. (mas yr^{-1})	−15.3(5)
Spin frequency, f (s^{-1})	207.96816335834(7)
$\dot{f}$ (s^{-2})	$-4.181(9) \times 10^{-16}$
Dispersion measure, DM (cm^{-3} pc)	13.35(3)
$\dot{DM}$ (cm^{-3} pc yr^{-1})	−0.001(5)
$\ddot{DM}$ (cm^{-3} pc yr^{-2})	−0.001(1)

[a]Ecliptic coordinates are used for PSR J1022+1001 and thus, ecliptic longitude λ and latitude β, and their proper motions are constrained.

[1]*Jodrell Bank Centre for Astrophysics, School of Physics and Astronomy, The University of Manchester, Manchester M13 9PL, UK*
[2]*Arecibo Observatory, HC3 Box 53995, Arecibo, PR 00612, USA*
[3]*Department of Physics, Lafayette College, Easton, PA 18042, USA*
[4]*National Radio Astronomy Observatory, PO Box O, Socorro, NM 87801, USA*
[5]*Space Science Division, Naval Research Laboratory, Washington, DC 20375-5352, USA*
[6]*Astrophysics Group, Cavendish Laboratory, JJ Thomson Avenue, Cambridge CB3 0HE, UK*
[7]*Centre for Astrophysics and Supercomputing, Swinburne University of Technology, Post Box 218 Hawthorn, VIC 3122, Australia*
[8]*National Radio Astronomy Observatory, 520 Edgemont Road, Charlottesville, VA 22903, USA*
[9]*Center for Research and Exploration in Space Science and Technology and X-Ray Astrophysics Laboratory, NASA Goddard Space Flight Center, Code 662, Greenbelt, MD 20771, USA*
[10]*ARC Centre of Excellence for Gravitational Wave Discovery (OzGrav), Swinburne University of Technology, Post Box 218 Hawthorn, VIC 3122, Australia*
[11]*Department of Physics and Astronomy, West Virginia University, P.O. Box 6315, Morgantown, WV 26506, USA*
[12]*Center for Gravitational Waves and Cosmology, West Virginia University, Chestnut Ridge Research Building, Morgantown, WV 26505, USA*
[13]*ASTRON, the Netherlands Institute for Radio Astronomy, Oude Hoogeveensedijk 4, Dwingeloo NL-7991 PD, the Netherlands*
[14]*International Centre for Radio Astronomy Research, Curtin University, Bentley, WA 6102, Australia*
[15]*Department of Astronomy and Cornell Center for Astrophysics and Planetary Science, Cornell University, Ithaca, NY 14853, USA*
[16]*Cornell Center for Advanced Computing, Cornell University, Ithaca, NY 14853, USA*
[17]*INAF – Osservatorio Astronomico di Cagliari, via della Scienza 5, I-09047 Selargius, Italy*
[18]*Canadian Institute for Advanced Research, CIFAR Azrieli Global Scholar, MaRS Centre West Tower, 661 University Ave. Suite 505, Toronto, ON M5G 1M1, Canada*
[19]*Kavli Institute for Astronomy and Astrophysics, Peking University, Beijing 100871, China*
[20]*Max-Planck-Institut für Radioastronomie, Auf dem Hügel 69, D-53121 Bonn, Germany*
[21]*Station de radioastronomie de Nançay, Observatoire de Paris, PSL Research University, CNRS/INSU, F-18330 Nançay, France*
[22]*Department of Time and Frequency, FEMTO-ST Institut de recherche, UBFC and CNRS, ENSMM, F-25030 Besançon, France*
[23]*Laboratoire de Physique et Chimie de l'Environnement et de l'Espace LPC2E CNRS-Université d'Orléans, F-45071 Orléans, France*
[24]*School of Physics and Astronomy and Institute for Gravitational Wave Astronomy, University of Birmingham, Birmingham B15 2TT, UK*
[25]*Department of Physics and Astronomy, University of British Columbia, 6224 Agricultural Road, Vancouver, BC V6T 1Z1, Canada*
[26]*CSIRO Astronomy, Space Science, Australia Telescope National Facility, PO Box 76, Epping, NSW 1710, Australia*
[27]*LESIA, Observatoire de Paris, Université PSL, CNRS, Sorbonne Université, University Paris Diderot, Sorbonne Paris Cité, 5 Place Jules Janssen, F-92195 Meudon, France*
[28]*Department of Physics, Hillsdale College, 33 E. College Street, Hillsdale, MI 49242, USA*
[29]*School of Chemistry, University of East Anglia, Norwich Research Park, Norwich NR4 7TJ, UK*
[30]*Department of Astronomy, University of Maryland, College Park, MD 20742, USA*
[31]*NASA Goddard Space Flight Center, Greenbelt, MD 20770, USA*
[32]*Department of Physics, McGill University, 3600 Rue University, Montréal, QC H3A 2T8, Canada*
[33]*McGill Space Institute, McGill University, 3550 Rue University, Montréal, QC H3A 2A7, Canada*
[34]*Physical Sciences Division, University of Washington Bothell, Bothell, WA 98011, USA*
[35]*Center for Gravitation, Cosmology & Astrophysics, Department of Physics, University of Wisconsin–Milwaukee, PO Box 413, Milwaukee, WI 53201, USA*
[36]*Department of Astrophysics/IMAPP, Radboud University, P.O. Box 9010, NL-6500 GL Nijmegen, the Netherlands*
[37]*Kavli Institute for Astronomy and Astrophysics, Peking University, Beijing 100871, China*
[38]*Canadian Institute for Theoretical Astrophysics, University of Toronto, 60 Saint George Street, 14th floor, Toronto, ON M5S 3H8, Canada*
[39]*CSIRO Astronomy and Space Science, Australia Telescope National Facility, PO Box 76, Epping 1710 NSW, Australia*
[40]*Center for Computational Astrophysics, Flatiron Institute, 162 Fifth Avenue, New York, NY 10010, USA*
[41]*Hungarian Academy of Sciences MTA-ELTE 'Extragalatic Astrophysics' Research Group, Institute of Physics, Eötvös Loránd University, Pázmány P. s. 1/A, Budapest 1117, Hungary*
[42]*Department of Physics, Università di Cagliari, S.P. Monserrato-Sestu Km 0,700, I-09042 Monserrato, Italy*
[43]*CSIRO Scientific Computing Services, Australian Technology Park, Locked Bag 9013, Alexandria, NSW 1435, Australia*
[44]*Dipartimento di Fisica, Universitá di Milano Bicocca, Piazza della Scienza 3, I-20126 Milan, Italy*
[45]*Department of Physics, Oregon State University, Corvallis, OR 97331, USA*
[46]*Jet Propulsion Laboratory, California Institute of Technology, Pasadena, CA 91109, USA*
[47]*TAPIR Group, California Institute of Technology, 1200 East California Boulevard, Pasadena, CA 91125, USA*
[48]*Department of Physics and Astronomy, Vanderbilt University, 2301 Vanderbilt Place, Nashville, TN 37235, USA*
[49]*Laboratoire Univers et Théories LUTh, Observatoire de Paris, PSL Research University, CNRS/INSU, Université Paris Diderot, 5 place Jules Janssen, F-92190 Meudon, France*
[50]*Key Laboratory of Radio Astronomy, Chinese Academy of Science, 150 Science 1-Street, Urumqi, Xinjiang 830011, China*
[51]*Purple Mountain Observatory, Chinese Academy of Sciences, Nanjing 210008, China*
[52]*University of Chinese Academy of Sciences, Beijing 100049, China*
[53]*National Astronomical Observatories, Chinese Academy of Sciences, A20 Datun Road, Chaoyang District, Beijing 100101, China*
[54]*CAS Key Laboratory of FAST, NAOC, Chinese Academy of Sciences, Beijing 100101, China*
[55]*OzGrav-Monash, School of Physics and Astronomy, Monash University, Clayton, VIC 3800, Australia*

This paper has been typeset from a TEX/LATEX file prepared by the author.